Supporting Information

Robust surface-to-mass coupling and turgor-dependent cell width determine bacterial dry-mass density

Enno R. Oldewurtel[1*], Yuki Kitahara[1,2,3], and Sven van Teeffelen[1,2*]

Table of Contents

SI Methods

1. Strain construction

To obtain strain S290 (MG1655/pDB192) the plasmid pDB192 (*bla* P_{lac}::*sulA*) (gift from Jun lab (University of California San Diego, CA) (1)) was transformed into MG1655 using TSS buffer (2).

2. Growth conditions

E. coli cell cultures were grown from an individual colony in LB Miller at 37C to exponential phase with appropriate selection of antibiotics. After growth in LB (to exponential phase or to saturation), cells were washed and diluted into LB Miller, defined MOPS minimal medium (MM) (MOPS Minimal Media Kit, M2106, Teknova) or MOPS Rich Defined Medium (RDM) (MOPS EZ Rich Defined Medium, M2105, Teknova). In MM we added mannose (0.4% w/v) (MM+mannose), glycerol (0.4% w/v) (MM+glycerol), glucose (0.2% w/v) (MM+glucose) or glucose (0.1% w/v) and BD Bacto casamino acids (0.1% w/v, Fisher Scientific, 11762764) (MM+glucose+CAA). Osmolality of MM and RDM was measured (Loeser, Freezing Point Osmometer) and adjusted using NaCl to be 280±10 mOsm. Osmolality of LB Miller medium was measured to be 390 mOsm.

C. crescentus cultures (strain CB15, obtained from Zemer Gitai lab) were grown to exponential phase from an individual colony in PYE medium (0.2% peptone, 0.1% yeast extract, 0.007% calcium chloride dihydrate w/v) at 30C to exponential phase.

Before microscopy, we kept cultures in exponential phase for >10 doublings. During this time we kept OD600 below 0.3 through back dilution, if necessary. If not otherwise indicated, cells were grown at 30C in liquid media in a shaking incubator. Strain S290 was grown with 50µg/ml carbenicillin. To inhibit division, *sulA* was induced with 1mM IPTG from plasmid pDB192 during microscopy.

For perturbations of cell shape, cell-wall synthesis, or metabolism we added the following compounds with concentrations indicated in Table S3: A22 (Cayman Chemical, #15870);2,4-dinitrophenol (DNP) (Sigma-Aldrich, D198501).

3. Microscopy

Microscopy was carried out on a Nikon Ti-E inverted phase-contrast and epi-fluorescence microscope. Additionally, we added a module allowing for spatial light interference microscopy (SLIM) (Fig. S3 and Supplementary Note 1). The microscope is equipped with a temperature chamber (Stage Top incubator, Okolab) set to 30C, a Nikon Plan Apo 100x NA 1.45 Ph3 Objective, a solid-state light source (Spectra X, Lumencor Inc., Beaverton, OR), a multiband dichroic (69002bs, Chroma Technology Corp., Bellows Falls, VT), and excitation (560/32) and emission (632/60) filters for FM4-64 imaging. Epi-fluorescence images were acquired with a sCMOS camera (Orca Flash 4.0, Hamamatsu) with an effective pixel size of 65nm, while phase-contrast and quantitative phase images were obtained with another CMOS camera (DCC3260M, Thorlabs) with an effective pixel size of 87nm. For experiments with *C. crescentus* we also took phase-contrast images using the Orca Flash 4.0 camera, as it provides higher-resolution images that are required to detect their smaller cell shape accurately.

For SLIM measurements we took six consecutive images with a phase delay of $\frac{n\pi}{2}$, where n = [1, 2, 3, 4, 1, 2], with 200 ms exposure each. Out of these, we obtained three phase images (from images 1-4, 2-5, and 3-6, respectively; Supplementary Note 1 Section 1) and took the average to obtain the final phase image. Including delays due to software, the acquisition of one final phase image took ~2 s. For

experiments with dividing cells, only individual cells up to their first division were analyzed. For snapshot experiments and for time-lapse experiments of filamenting cells (*sulA* induced), only non-dividing cells were analyzed. We consider cells to be dividing if curvature on opposite sides of the same cell is smaller than 1/(75 contour points) for 3 consecutive contour points (contour points obtained from Morphometrics). The curvature threshold value was chosen empirically. Non-dividing cells can be modelled as spherocylinders.

4. Sample preparation

Images were obtained by immobilizing cells either under an agar pad or inside a flow chamber as described below. In all experiments care was taken to image individual cells that are well-separated from any neighboring cells. This is to ensure proper segmentation and integration of optical phase. All snapshot images (single-time-point measurements) were conducted on agar pads (for numbers of cells per experiments see Table S2). Time-lapse experiments were conducted either on agar pads or in flow chambers, as indicated in Table S3. Agar pads had the advantage of better cell immobilization. However, for cells on agar pads made from minimal media we observed faster than expected growth, demonstrating that the agar pads contain additional nutrients. For example, the biomass growth rate of cells growing on MM+Mannose was about 0.22/h in liquid channels and in bulk (the latter according to OD600) but increased from 0.44 to 0.51/h during the first 20 min of growth on agar pads. Time-lapse movies on agar pads were therefore taken only for amino-acid-supplemented media (MM+glucose+CAA or RDM).

Agar pads: Agar pads were prepared from fresh culture medium and 1% or 1.2% UltraPure Agarose (16500-500, Invitrogen) for *E. coli* and *C. crescentus*, respectively. For microscopy, 1ul of cell culture with OD_{600}~0.1 was directly applied onto a coverslip (Corning No 1.5), which was already assembled on the microscope and inside the stage-top incubator. The droplet was then immediately covered with an agar pad. Optical alignment and focus position had been done before using a separate agar pad. Therefore, imaging could be started as early as 0.5-1.5 min after taking cells from the shaking incubator.

To measure cell dimensions with the membrane stain FM4-64 (ThermoFisher, T13320) for the calibration of shape measurements from phase-contrast images (see Supplementary Note 1), we prepared agar pads containing 1% or 1.2% UltraPure agarose, MM+mannose or RDM for *E. coli*, PYE for *C. crescentus*, and 20ng/ml FM4-64. To avoid fluorescent signal from dirt on the coverslip we pre-cleaned cover slips by bath sonication in a 1M KOH solution for 1h at 40C. Images were acquired only after ~10min exposure to FM4-64, when maximum fluorescent signal was reached.

For treatments with A22 or DNP using agar pads (Table S3), the drug was already contained in the agar pad, i.e. cells were grown in RDM in liquid and exposed to A22 or DNP once they were covered with the agar pad. For the osmotic ramp experiments (Fig. 6; Fig. S21), we grew cells in osmolality adjusted medium as indicated in Table S3, we then immobilized cells under a microscopy agar pad with thickness h_1 as indicated in Table S3, and eventually placed a second agar pad with thickness h_2 on top. This leads to a slow change in osmolality due to the NaCl concentration equilibrating via diffusion. Based on a one-dimensional diffusion model, we predicted the change in osmolality (Fig. 6; Fig. S21).

Flow chambers: For time-lapse experiments in flow chambers we used commercial flow chambers (sticky-slide I Luer 0.2, Ibidi) and provided constant flow of media of 50 ul/min via connected silicone tubings using a syringe pump (70-4501, Harvard Apparatus). For osmotic shock experiments we used flow chambers (sticky-slide I Luer 0.1, Ibidi) with a flow of 300 ul/min. To attach cells to the surface, 24x60 mm coverslips (Corning No 1.5) were pre-treated with APTES ((3-Aminopropyl)triethoxysilane, Sigma-Aldrich, A3648-100ML). Specifically, coverslips were incubated with 2% APTES in EtOH

(vol/vol) for 15 min at RT, 3x washed in EtOH, rinsed with distilled water and finally stored in EtOH. Before use, coverslips were again rinsed with water and dried with compressed air.

We did not observe any apparent reduction of single-cell growth rate

Flow chambers were assembled on the microscope and filled with 100 ul of cell suspension with OD_{600}~0.1. Cells were allowed to settle for ~5 min. Shift experiments in flow chambers were conducted by using a Y-junction about 5 cm upstream of the channel and switching the flow from syringe #1 (containing medium #1) to syringe #2 (containing medium #2). To avoid leakage of medium #2 into the feeding channel prior to the shift, both inlets of the Y-junction were filled with medium #1 prior to the shift.

5. Immersive refractometry and volume-independent measurement of average refractive index

Refractive-index modulation: We imaged cells using SLIM but increased the refractive index of the surrounding medium. If the cell or part of the exhibits a positive phase shift, the cell has a higher refractive index than the surrounding medium. If the cell shows a negative phase shift, the cell has a lower refractive index of the medium. This technique is independent of volume measurements and does not require any correction of the SLIM measurement. The same qualitative behavior is also seen in phase-contrast images (3). For measurements displayed in Fig. S7, MG1655 cells were grown in MM+glucose or in RDM. BSA (Sigma-Aldrich, A2153) was dissolved in fresh MM+glucose medium to increase the refractive index to n_{medium}=1.384. Media without and with BSA were adjusted to equal osmolality (~280mOsm). Cells were then immobilized in a flow chamber containing either MM+glucose or RDM. Subsequently, the growth medium was replaced with MM+glucose+BSA. To compare cells grown in either MM+glucose or RDM in a medium of the same refractive index, we used the same MM+glucose+BSA medium for both cultures.

Immersive refractometry: Following a different technique to measure the average refractive index of a cell directly (4), without using the information about cell shape, we obtained phase images of the same cell for two different media with different refractive indices (Figs. S4, S9; Supplementary Note 1). To increase refractive index, we used high-molecular weight dextran (200kD, 31398, Sigma). Osmolalities of low and high refractive index medium were matched by addition of NaCl (~280mOsm). We exchanged media multiple times, which allowed to measure both the length dependency of dry-mass density between different cells and the decrease of dry-mass density in individual filamenting cells over time.

6. Analysis of shape and mass during time-lapse microscopy

We filtered time traces of mass, length, width, surface, and volume using a Gauss filter of standard deviation σ as indicated in Table S3. For the display of relative changes of mass, volume, surface and other quantities from time-lapse microscopy (see, e.g., Fig. 3E), we linearly extrapolated single-cell quantities to $t = 0$, the start of the perturbation, unless indicated otherwise.

For those measurements where we sought to obtain quantities as fast as possible after sample preparation, we used an average filter of width *N* instead (smooth function, MATLAB) (see also Table S3).

Relative rates $\lambda_X = \mathrm{d}(\log X)/\mathrm{d}t$ $(X = S, W, L, M)$ with measurement time points t_i were calculated as

$$\lambda_X(t_{i+1/2}) = \frac{2(X_{i+1} - X_i)}{(X_{i+1} + X_i)\Delta t_i},$$

where $t_{i+1/2} = 0.5(t_i + t_{i+1})$. Before display, rates were smoothened with the same filter used for quantities X. As a consequence of smoothening, rates seem to change shortly before the timepoint of a shift. For the quantities $\alpha = \mathrm{d}S/\mathrm{d}M$ and $\beta = \lambda_M \alpha$ (Fig. 5, Fig. S20), we first filtered time traces of raw mass and surface using an average filter of width $N = 9$ (smooth function, MATLAB). Then, we calculated

$$\alpha(t_{i+1/2}) = \frac{(S_{i+1} - S_i)}{(M_{i+1} - M_i)}$$

and subsequently smoothened with the same average filter of width $N = 9$. We obtained $\beta(t_{i+1/2}) = \alpha(t_{i+1/2})\lambda_M(t_{i+1/2})$ and subsequently smoothened with the same filter.

7. Conversion of literature values to dry-mass density

In Fig. 1D,E we compare our dry-mass density measurements with bulk measurements of wet-mass density (Fig. 1D) and radio-chemically labelled free water measurements (Fig. 1E).

Wet-mass density, also called buoyant mass density, was reported for *E. coli* growing in LB for early exponential growth phase and after 24h for stationary phase cells (5) to be around $\rho_{\mathrm{wet}} = 1.087$ and 1.110 g/ml, respectively, that is, wet-mass density increases in stationary-phase cells. Wet-mass density is defined as $\rho_{\mathrm{wet}} = M_{\mathrm{tot}}/V$, with $M_{\mathrm{tot}} = M_{\mathrm{dry}} + M_{\mathrm{H2O}}$ the total mass of the cell containing dry mass and water. Wet-mass density and dry-mass density are related according to

$$\rho_{\mathrm{wet}} = \rho + \frac{M_{\mathrm{H2O}}}{V} = \rho + \frac{\rho_{\mathrm{H2O}} V_{\mathrm{H2O}}}{V} = \rho + \frac{\rho_{\mathrm{H2O}}}{V}\left(V - V_{\mathrm{dry}}\right).$$

Introducing the average specific density of dry mass $\rho_{\mathrm{dry}} = M_{\mathrm{dry}}/V_{\mathrm{dry}}$ we then get

$$\rho_{\mathrm{wet}} = \rho + \frac{\rho_{\mathrm{H2O}}}{V}\left(V - \frac{M_{\mathrm{dry}}}{\rho_{\mathrm{dry}}}\right) = \rho\left(1 - \frac{\rho_{\mathrm{H2O}}}{\rho_{\mathrm{dry}}}\right) + \rho_{\mathrm{H2O}}\,.$$

Dry-mass density shown in Fig. 1D is then obtained as

$$\rho = \frac{\rho_{\mathrm{wet}} - \rho_{\mathrm{H2O}}}{1 - \frac{\rho_{\mathrm{H2O}}}{\rho_{\mathrm{dry}}}}.$$

The average specific density of dry mass is around $\rho_{\mathrm{dry}} = 1.45$ g/ml and 1.39 g/ml for *E. coli* in LB in early exponential growth and stationary phase, respectively (6).

Radio-chemical free water measurements were reported for *E. coli* growing in MM+glucose at various growth osmolalities, for which the amount of free (accessible) water per dry weight ($\overline{V_{\mathrm{cell}}^{\mathrm{wa}}} = V_{\mathrm{H2O}}/M_{\mathrm{dry}}$) and the water-inaccessible cell volume ($\overline{V_{\mathrm{cell}}^{\mathrm{wi}}} = V_{\mathrm{dry}}/M_{\mathrm{dry}}$) was measured (7). The latter was found to be independent of external osmolality and is related to the average specific density of dry mass, $\rho_{\mathrm{dry}} = 1/\overline{V_{\mathrm{cell}}^{\mathrm{wi}}} = 1.59\mathrm{g/ml}$. Finally, dry-mass density values shown in Fig. 1E are inferred using: $\rho = \rho_{\mathrm{dry}}/(1 + \rho_{\mathrm{dry}}\overline{V_{\mathrm{cell}}^{\mathrm{wa}}})$.

Supplementary Note 1 – Quantitative Phase Microscopy

1. Microscope setup

For dry-mass measurements we used Spatial Light Interference Microscopy (8), which we added to a Nikon Ti-E microscope using custom components (Fig. S3). The Nikon Ti-E is equipped with typical phase-contrast illumination with illumination confined by an annulus (Ph3) in the condenser (ELWD NA 0.52) and a matching phase-ring in the pupil plane of the objective (Plan Apo 100x 1.4 Ph3). To fully illuminate the condenser aperture, we added a 2x telescope to the illumination arm of the Ti-E (LC1315-A and LA1417, Thorlabs). The pupil plane of the objective is relayed via a fourier lens (AC508-300-A, Thorlabs) onto a spatial light modulator (SLM, Meadowlarks P1920) where a matching phase ring is displayed. This allows to modulate the phase ring (see below for details). Another fourier lens (AC508-200-A, Thorlabs) completes the first optial 4f-configuration. Another 4f-configuration (two AC508-200-A lenses, Thorlabs) is used to access the pupil plane again, where an iris aperture (Thorlabs) limits the objective numerical aperture to N.A.~0.6. Finally, a set of long and short pass filters (FEL0600 and FES0700, Thorlabs) restricts light transmission to 600-700nm, which in combination with the power spectrum of the illumination LED gives a center wavelength of ~635nm. The image plane is then projected onto the camera. Finally, a linear polarizer (LPVISE200-A, Thorlabs) is placed near the image plane at the exit port of the microscope and orientated with the SLM to act in "phase modulation" mode.

The microscope and display of the SLM monitor were controlled via MATLAB. Micro-manager (9) was used to control the Nikon Ti-E microscope and acquire images from the camera from within MATLAB.

2. Spatial Light modulator calibration and phase modulation

The SLM is connected via HDMI to a PC and acts like a second monitor such that the image displayed on the second monitor is fed to the SLM and the gray-value signal of each pixel on the monitor controls the corresponding pixel on the SLM. The phase delay imparted by the SLM was calibrated as described in (8). Briefly, a linear polarizer was placed 45° to the active axis of the SLM, such that it works in "amplitude modulation" mode. The transmitted intensity during a gray-value sweep was recorded and the phase delay was obtained via a Hilbert transform of the amplitude response (Fig. S22):

Furthermore, we confirmed a sufficiently long coherence length of the illuminating white light (Fig. S23A) by retrieving the autocorrelation from its optical spectrum as the full width at half maximum of the envelope (black horizontal bar in Fig. S23B), giving $l_c^{\mathrm{FWHM}} = 4.7$ um and several full cycle modulations in the flat part near the central peak. This allows the application of the phase shifting procedure in SLIM (10, 11).

3. Optical phase retrieval

The optical phase shift of light travelling through the cell can be obtained from 4 intensity images as outlined in (8, 11–13). Conceptually, the total optical field U_t emanating from the sample can be decomposed into the incident field U_i and scattered field U_s (13). In phase-contrast microscopy, these fields are mainly spatially separated in the pupil plane of the objective: U_i passes through the phase ring, while U_s mainly passes outside the phase ring. Due to the presence of the phase-ring in the objective and again on the SLM, the incident field can be phase-shifted with respect the scattered field. For SLIM this is done in increments of $\pi/2$ such that the total field becomes:

$$U_t(x,y;n) = U_i e^{i\frac{n\pi}{2}} + U_s(x,y).$$

Here, *n* is the number of π/2 increments due to phase ring and SLM ring. The image I_n on the detector is the result of the interference of $U_i e^{i\frac{n\pi}{2}}$ and U_s:

$$I_n(x,y) = |U_i e^{i\frac{n\pi}{2}} + U_s(x,y)|^2 = |U_i|^2 + |U_s(x,y)|^2 + 2|U_i||U_s(x,y)|\cos\left(\Delta\varphi(x,y) + \frac{n\pi}{2}\right),$$

where $\Delta\varphi(z,y) = \varphi_i - \varphi_s(x,y)$. With $\varphi_{i/s/t}$ we refer to the phases of the incident, scattered, and total fields, respectively, that is, $U_{i/s/t} = \left|U_{i/s/t}\right|e^{i\varphi_{i/s/t}}$. $I_n(x,y)$ is obtained directly from the camera images after correcting for background signal. As a background image we took the average over 100 images under dark conditions.

The aim of SLIM is to retrieve the optical phase shift of the cell with respect to the incident light, $\varphi = \varphi_i - \varphi_t$. φ is obtained as

$$\varphi = \arg\left(\frac{\beta\sin(\Delta\varphi)}{1+\beta\cos(\Delta\varphi)}\right),$$

where $\Delta\varphi$ is the phase shift between U_i and U_s and β is the ratio of field amplitudes $|U_s|/|U_i|$. Following ref. (12), $\Delta\varphi$, in turn, is obtained as

$$\Delta\varphi = \frac{I_3 - I_1}{I_4 - I_2}$$

and β is obtained as

$$\beta = \gamma\,\frac{1}{4I_i}\frac{I_4 - I_2 + I_3 - I_1}{\sin(\Delta\varphi) + \cos(\Delta\varphi)}.$$

Here, γ accounts for the amplitude attenuation of the phase ring in the objective. To measure γ we imaged the back-focal plane upon even (brightfield) illumination using a Bertrand lens and measured the image intensity inside and outside the attenuation ring. In the case of the objective used here (Nikon 100x 1.45 Ph3), we found the amplitude attenuation to be $\gamma = \sqrt{0.1}$.

The illumination intensity I_i in the expression for β is obtained as

$$I_i = \frac{g + \sqrt{g^2 - 4L^2}}{2}.$$

Here, g and L are defined as

$$g = \frac{I_1 + I_2 + I_3 + I_4}{4},$$

$$L = \frac{1}{4}\frac{I_4 + I_3 - I_2 - I_1}{\sin(\Delta\varphi) + \cos(\Delta\varphi)}.$$

I_i should be homogenous across the field of view, but the estimate I_i tends to be biased near the presence of phase objects. To avoid bias on the estimate of I_i at or near a cell, the pixels within ~4 um distance of any phase object are excluded and I_i is inferred from the surrounding area of every cell. The distance of 4 um was chosen empirically to make sure that the phase object does not affect background calculation. Specifically, the intensity field I_i is smoothened before exclusion of phase objects. Then, the intensity

values inside regions of phase objects is interpolated. The process of phase retrieval is also illustrated in Fig. S2.

4. Increased focal depth to measure full phase delay

The optical setup contains an iris aperture to limit the NA of the objective (position in the second 4f-configuration, conjugate to the pupil plane). Thus, the focal depth is increased, and the phase signal can be obtained for the entire cell. The integrated phase signal of a 370nm polystyrene bead with increasing defocus dz is plotted in Fig. S24. Given the small variation of <1% for $|dz|$<0.4um and taking into account the dimension of the bead, this indicates that the total phase shift imparted by a cell can be measured for cells with a diameter of up to ~1.2 um. Larger defocusing indicates that even the phase shift of an object of ~2.4 um diameter would still be measured to more than >90%. Accordingly the phase of a bead measured at different focal positions is.

5. Optical path-length noise level

SLIM has been shown to exhibit a low background noise level (8). To demonstrate this we measured the phase signal inside a flow chamber filled with water, but 100 um away from the coverslip (Fig. S25). This should demonstrate the intrinsic noise level associated with our setup irrespective of the biological sample. We find a uniform background across nearly the entire field-of-view with a standard deviation in the measured optical path-length of std = 0.001 rad. This is <0.01% of the integrated phase shift of a typical cell.

6. Cell shape and volume measurements and corrections

Cell dimensions were obtained from phase-contrast images acquired using the SLIM module (Fig. S3) or the epi-fluorescence port, for *E. coli* and *C. crescentus*, respectively. Images obtained on the epi-fluorescence port are sharper due to the higher NA of 1.45 and proved important for proper cell segmentation in case of the smaller and crescent-shaped *C. crescentus* cells.

We used the MATLAB based tool Morphometrics (https://simtk.org/projects/morphometrics), (14) to determine cell contours. The image-formation process through the microscope, but also the contour-finding routines of Morphometrics can bias and distort the contour. We correct and calibrate for this as follows: We base our calibration on images of cells stained with the fluorescent membrane stain FM4-64, which stains predominantly the outer membrane (15). These images were acquired using the epi-fluorescence port of the microscope. To position cells reproducibly at the focal plane of the microscope, we first used the automatic positioning system of the perfect focus system (PFS) of the Nikon-TiE microscope followed by subsequent visual maximization of contrast of both phase-contrast and FM4-64 images obtained on the epi-fluorescence port. This procedure led to reproducible results during replicates.

To correct for diffraction, we also simulated membrane-stained cells using the MATLAB based tool BlurLab (https://simtk.org/projects/blurlab/) (14). To this end we acquired the point-spread function (PSF) from 100nm fuorescent beads (TetraSpeck, Thermo Fisher) and used BlurLab to convolve point emitters sitting on the surface of a sphero-cylinder, with the PSF. We applied the correction found in silico onto the measured membrane contours to obtain an estimate for the true contour of the periphery of the cell. In addition to the epi-fluorescence images, we obtained phase-contrast images of the same cells using the SLIM module (for *E. coli*) or the epi-fluorescence port (for *C. crescentus*). We then overlaid the measured contour of the phase-contrast cell with the corrected membrane contour obtained

from the membrane dye and found the radial offset between the two (grey lines in right panel of Fig. S1).

In *E. coli*, we used the camera on the SLIM setup for this task. Doing this comparison for n>1000 cells grown in MM+mannose and in RDM, we inferred an average correction as a function of distance from the cell pole. We found no significant dependence on cell width and growth medium and therefore only applied corrections as a function of distance from the pole. This correction was used to correct the contours of all cells measured with the SLIM module.

In *C. crescentus* we similarly overlaid the contour of the phase-contrast cell, but now found from phase-contrast image of the epi-fluorescent port, and the corrected membrane contour. Using the epi fluorescence port helped to resolve the smaller *C. crescentus* cells more accurately. This comparison was done for cells grown in PYE and PYE+A22, respectively. Congregating all conditions into one analysis, we found the radial offset to depend both on distance from the cell pole, as well as the 2nd principal curvature of the cell contour. Thus, for *C. crescentus* the contour correction is applied both as a function of distance from the pole, as well as the 2nd principal curvature.

The corrected contours are used to determine cell dimensions and are also used for the simulation of phase images.

Our calibration method allows us to correct the measured contours from phase-contrast images such that they represent the absolute dimensions of the cell. However, since we calibrated during steady-state growth conditions, we cannot rule out that the method reports cell dimensions that differ from the dimensions of the outer membrane in case the cytoplasmic biomass distribution is highly perturbed, such as during plasmolysis. However, even during the plasmolysis shown in the A22 timelapse (Fig. 3D-E), the contour is still found on the edges of the periplasm.

Finally, given the calibrated contours of the cell, we use Morphometrics to apply a mesh-grid of 1px (87nm) step-size. This routine also gives the centerline of the cell, which is used to determine cell length. We then assume cylindrical symmetry around the centerline and infer cell surface and cell volume from the sum of the surfaces and volumes of truncated conical wedges with height and width given by the meshes (Fig 1B).

7. Correction of phase signal via comparison with simulated images

The calculation of the optical phase outlined in Supplementary Note 1 Section 3 assumes complete separation of incident field and scattered field at the Fourier plane (i.e., in the plane of the objective phase ring and the plane of the SLM). However, as a consequence of the finite thickness of the phase ring, low spatial frequency components of the scattered field leak into the ring and are incorrectly phase-modulated. For the same reason phase-contrast images are typically plagued with halos and shade-off artifacts. Thus depending on the shape of the phase object, the phase φ is under-estimated (13), and thus also the integrated phase ϕ:

$$\phi = \int_{\varphi>0} \varphi \mathrm{d}x\mathrm{d}y.$$

To correct for the underestimate in ϕ, we simulate phase images. Simulations are based on the optical parameters of our microscope, like size and thickness of the phase ring, illumination ring and attenuation of the phase ring, which we could all measure directly by imaging the pupil plane of the objective. The simulations are then performed following the description for phase-contrast microscopy (16, 17) and SLIM (13), aided by available software packages (https://github.com/mehta-lab/microlith;

https://github.com/thnguyn2/Halo_removal_with_two_gammas). Briefly, partially coherent image formation can be described as the summation of images illuminated from coherent point sources, which are positioned on the illumination ring. It is possible to simulate the image formation from an input ground-truth to the measured image without any free parameters, solely based on the measured parameters of the microscope. To decrease computational cost of the simulation, we limited the number of point sources on the illumination ring to 75. These were evenly distributed across the illumination ring. We verified that increasing the number of points did not change the phase signal of the simulated cell.

For each cell and every time-point, we take the measured contour of the cell, assume cylindrical symmetry around its centerline to simulate a phase-object of the same shape and size as the measured cell. For simplicity, we assume a constant refractive index difference inside the cell ($\Delta n = n_{\mathrm{cell}} - n_{\mathrm{medium}}$; c.f. Fig. 1B). For a discussion of the validity of this assumption see the subsequent paragraph. The aim of the simulation is to estimate the attenuation of the integrated phase by comparing the initial integrated phase of the input, $\phi_{\mathrm{sim,input}}$, with the integrated phase of the output of the simulation, $\phi_{\mathrm{sim,output}}$ (Fig. S1). The integrated phase of the measured cell, ϕ_{meas}, is then corrected for the attenuation found from the simulation:

$$\phi_{\mathrm{corr}} = \phi_{\mathrm{meas}} \frac{\phi_{\mathrm{sim,input}}}{\phi_{\mathrm{sim,output}}} .$$

The corrected integrated phase ϕ_{corr} is then used for the calculation of dry mass as outlined in Supplementary Note 1 Section 8.

For our simulations we assume a constant intracellular refractive index. However, in real cells, the intracellular refractive index is not constant (18), and an inhomogeneous distribution of mass inside the cell will affect the distribution of the phase signal φ. However, our simulations showed that the total integrated phase ϕ was constant within <0.4 % for different ways to distribute dry mass inside the cell, for example if we simulated cells with a 150nm shell of 5x higher mass-density than its inner core (simulated cell with L = 3.5µm, W = 0.88µm). Furthermore, the attenuation of the phase was constant within <1 % if we varied Δn up to 30%. To minimize the effect of differences between Δn used in the simulation and Δn of the experimental sample, we adjusted Δn such that the average phase $\langle \varphi_{\mathrm{sim,output}} \rangle_{(x,y)\in A}$ matches the average phase $\langle \varphi_{\mathrm{meas}} \rangle_{(x,y)\in A}$ inside the cell area A obtained from the measured phase-contrast image.

Our simulation also revealed the attenuation of the integrated phase to be robust against small variation in cell shape, i.e. the attenuation was constant within <0.6% for 100nm variations in both length and width (see also Fig. S26). However, the shape-dependent correction becomes important for larger variations in shape (Fig. S26), e.g., the attenuation changes by >10% for cells grown in MM+Mannose (L = 2µm, W = 0.72µm) vs. RDM (L = 4.1µm, W = 0.98µm).

8. Conversion of phase shift to cellular dry mass

The concept to relate refractive index to the dry-mass density of a cell has been proposed by Barer (19). This idea relies on the assumption that the refractive index of a cell is proportional to its dry matter content:

$$n_{\mathrm{cell}} = n_{\mathrm{H2O}} + \gamma \rho ,$$

where $\rho = M_{\mathrm{dry}}/V_{\mathrm{cell}}$ is the average concentration of dry matter of the cell. γ is a proportionality constant called the refraction increment, which reflects the average composition of the cell. The linear relation between the refractive index difference n_{cell} - n_{H2O}, and mass density has been shown for well-

mixed solutions of different solutes over a wide range of concentrations (20, 21). According to our own osmotic-shock experiment (Fig. 1C) and to similar experiments in HeLa cells (22), a linear relationship between n_{cell} - n_{H2O} and mass density apparently also holds for the complex interior of a cell. We use an average refraction increment, which we obtained by considering the reported composition of dry-mass (23) and reported values for the refraction increments (Table S5).

Within the uncertainty in the values of the refraction increments for the individual constituents of the cell, the weighted average refraction increment is around 0.174 – 0.181 ml/g. To account for the higher illumination wavelength of 635nm used in our experiments, we further decrease the refraction increment by 1% (20). Thus, we arrive at the average refraction increment of $\gamma = 0.175$ ml/g, which we used for all conversions.

Dry-mass composition given in Table S5 was obtained from the *Escherichia coli* B/r strain grown in MM+glucose (23). However, composition changes as a function of growth rate (28), with mass fractions of DNA (3.7%), RNA (11.9%), Protein (64.2%) in a poor Alanine-based medium, and DNA (1.9%), RNA (29.4%), protein (48.7%) in a rich Tryptone-yeast based medium (28). Assuming that the composition of the remaining dry weight stays similar, the average refraction increment changes by ~1% between poor and rich medium. Since this change is much smaller than the effect sizes observed in our shift experiments, we assume a constant average refraction increment for all growth conditions. While the absolute accuracy of the refraction increment dominates the uncertainty of our absolute mass and dry-mass-density measurements, all our conclusions are based on relative changes of dry mass or dry-mass density.

Dry mass is then obtained from the integrated phase ϕ_{corr} (see Suplemental Note Section 7) plus a correction due to the refractive index of the medium, n_{medium}, which is higher than the refractive index of water, n_{H2O}:

$$M_{\mathrm{dry}} = \frac{1}{\gamma}\left[\frac{\lambda}{2\pi}\phi_{\mathrm{corr}} + V_{cell}(n_{\mathrm{medium}} - n_{\mathrm{H2O}})\right].$$

Here, λ is the central wavelength. For our experiments, we measured refractive index n_{medium} at 20C using a refractometer (Brix/RI-Chek, Reichert) and used $n_{\mathrm{H2O}} = 1.33299$. In case of agar pad experiments we added n_{agar}=0.0015 to n_{medium}, based on our refractive-index measurements of a solution of 1% Ultrapure agarose in LB and in agreement with (29).

9. Precision of shape and mass measurement of fixed cell

To assess the precision of our shape and dry-mass measurements, we fixed MG1655 cells grown in RDM by treating with 3.7% formaldehyde for 20 min at room temperature. After washing with PBS we imaged cells on an agar pad (1% Ultrapure agarose in PBS). Single-cell precision of shape and mass measurements show a coefficient of variation of CV<0.2%, with dry-mass measurements showing CV=0.06%. This indicates that our implementation of SLIM and subsequent processing to dry mass surpasses the implementation of SLIM reported by Mir et al. (30).

10. Exponential growth in dry mass with correction factor from simulation

The importance of the correction factor derived from simulated images (Supplementary Note 1 Section 7) can nicely be seen following the growth dynamics of exponentially growing bacteria. Cells grow exponentially in mass (31). We also see exponential growth in dry mass (Fig. 2E), but only after

correction from the simulation. Without correction the integrated phase does not show constant exponential growth due to the shape-dependent correction factor (Fig. S27).

11. Calculation of average refractive index based on media with different indices

Comparison of the integrated phase shift ϕ_1 and ϕ_2 obtained from the same cell, but in two different media of different refractive indices allows to deduce the average refractive index n_{cell} as follows (4):

$$\phi_1 = \frac{2\pi}{\lambda}(n_{\mathrm{cell}} - n_{\mathrm{medium}})V_{\mathrm{cell}}$$

$$\phi_2 = \frac{2\pi}{\lambda}(n_{\mathrm{cell}} - n_{\mathrm{medium}} + \delta_{\mathrm{Dextran}})V_{\mathrm{cell}}$$

$$n_{\mathrm{cell}} = \frac{\delta_{\mathrm{Dextran}}\phi_1}{\phi_1 - \phi_2} + n_{\mathrm{medium}}$$

Here, $\delta_{\mathrm{Dextran}}$ is the refractive index difference due to dextran and n_{medium} is the refractive index of the medium without dextran. We convert n_{cell} to dry-mass density using a refraction increment of $\gamma = 0.175$ ml/g.

Supplementary Note 2 – Model of mass density of elongating cells

To model the length dependency of dry-mass density and volume growth rate of filamenting, non-dividing cells, we assumed a spherocylinder of width W, which increases its surface S in direct proportion to mass M, with a ratio S/M given by the average experimental value (Fig. 2C). Surface and volume of a spherocylinder are given by $S = \pi WL$, $V = \pi W^2(L - W/3)/4$. Therefore, the surface-to-volume ratio S/V decreases with increasing length according to

$$\frac{S}{V} = \frac{4}{W[1-W/(3L)]}. \tag{1}$$

Dry-mass density can then be written as $\rho = (S/V)/(S/M)$, which is directly proportional to S/V for constant S/M.

For our deterministic model, we assumed that $\langle\rho\rangle = \langle S/V\rangle/\langle S/M\rangle$, thus ignoring single-cell correlations between S/V and S/M. This approach is justified, because relative fluctuations in both quantities are smaller than 5% (Fig. 2). According to Cauchy-Schwarz we get

$$|\langle\rho\rangle - \langle S/V\rangle\langle(S/M)^{-1}\rangle| = |\mathrm{Cov}(S/V, (S/M)^{-1})| \leq \sqrt{\mathrm{Var}(S/V)\mathrm{Var}((S/M)^{-1})}\,.$$

With standard deviations of both S/V and $(S/M)^{-1}$ smaller than 5%, the contribution of correlated fluctuations to variations of $\langle\rho\rangle$ is at least 10-fold smaller than the deterministic dependency on length.

Constancy of S/M implies that surface and mass growth rates are equal, $\lambda_S = \lambda_M$. Since the surface of a spherocylinder (and of dividing spherocylinders) is equal to $S = \pi WL$, elongation rate and surface rates are also equal. On the contrary, the volume growth rate is different from the surface rate. It can be obtained as

$$\lambda_V = \frac{S}{V}\frac{\mathrm{d}V}{\mathrm{d}S}\lambda_S = \frac{\lambda_S}{1-W/(3L)}, \tag{2}$$

where we used $\mathrm{d}V/\mathrm{d}S = (\pi W)^{-1}\mathrm{d}V/\mathrm{d}L = W/4$.

In Fig. 2E, we present the volume rate as a function of time, considering at every time point the smoothened average cell length and width, and a constant surface growth rate λ_S. With experimental average dimensions of $\langle L\rangle_{20\mathrm{min}} = 3.43$ um, $\langle W\rangle = 0.83$ um after 20 min we obtained $\lambda_V = 1.08\,\lambda_S$. Since not all cells start out with the same initial length, we confirmed that $\lambda_V(\langle L\rangle)$ was almost identical to $\langle\lambda_V(L)\rangle$.

Supplementary Note 3 – Model of turgor pressure during osmolality ramp

Here, we use a simple model of osmoadaptation to show that under simplifying but reasonable assumptions turgor pressure and osmolality ramp rate are approximately proportional to one another at long times into a ramp. Accordingly, the experimentally observed correlations between widening rate and ramp rate then suggest that widening rate might be approximately proportional to turgor pressure. Specifically, we assume that cells undergo osmoadaptation according to the following time evolution for the cytoplasmic osmolyte concentration c,

$$\dot{c} = -k(\Delta c - \Delta c_0). \tag{1}$$

Here, $\Delta c = c - c_{\mathrm{ext}}$ is the difference in concentration between the cell and the extracellular environment, where c_{ext} is the time-varying NaCl concentration at the position of the cells. Δc_0 is the preferred concentration difference. For simplicity, we don't distinguish different molecular species contributing to turgor and we assume that turgor pressures P is proportional to Δc according to $P = \Delta c RT$, with RT the thermal energy. Furthermore, we assume implicitly that transport or synthesis of osmolites during a ramp dominate changes in osmolyte concentration, while cell-volume changes play a minor role.

The osmolality ramps realized using agarose pads (Fig. 6; Fig. S21) asymptotically approach an exponential decay of the form $c_{\mathrm{ext}} \cong (c_1 - c_2)\exp(-\gamma t) - c_2$ with $\gamma = \pi^2 D/h^2$ shortly after the beginning of the experiment (for $t \gg \frac{L^2}{4\pi^2 D} \approx 4 - 9$ min). Here c_1 and c_2 are initial and final concentrations, respectively, $h = h_1 + h_2 =$ 4-6 mm is the total height of the two pads, and $D =$ 1.6e-5 cm^2/s is the average diffusion constant of NaCl in water (32). This result is obtained by solving a one-dimensional diffusion equation through Fourier decomposition, in complete analogy to ref. (33). The time evolution of Δc can then be solved analytically as

$$\Delta c = \Delta c_0 + c_2 + \frac{c_1 - c_2}{k - \gamma}(k e^{-\gamma t} - \gamma e^{-kt}) = \Delta c_0 + \frac{1 - e^{-(k-\gamma)t}}{k - \gamma}\frac{\mathrm{d}c_{\mathrm{ext}}}{\mathrm{d}t}.$$

We don't know the effective rate of osmoadaptation k in absolute terms. However, the hyperosmotic ramp (Fig. 6) reveals that cell width recovers partially after an initial drop, about 20 min after the beginning of the experiment. This recovery suggests a partial restoration of turgor after the initial, rapid increase of c_{ext}, indicating that the time scale of osmoadaptation is smaller than 20 min and faster than the ramp rate. Under this assumption, we obtain for long times ($t \gg (k - \gamma)^{-1}$):

$$\Delta c - \Delta c_0 \simeq (k - \gamma)^{-1}\frac{\mathrm{d}c_{\mathrm{ext}}}{\mathrm{d}t}. \tag{2}$$

To zeroth order in γ, the model thus predicts a linear relationship between turgor P and instantaneous ramp rate $\frac{\mathrm{d}c_{\mathrm{ext}}}{\mathrm{d}t}$:

$$P - P_0 \simeq \zeta\frac{\mathrm{d}c_{\mathrm{ext}}}{\mathrm{d}t}. \tag{2}$$

Here, P_0 is the adapted pressure corresponding to the concentration difference Δc_0, and $\zeta = RT/k$. The instantaneous experimental correlations between widening rate and ramp rate are thus compatible with a straight-forward linear relationship between plastic cell widening and pressure:

$$\frac{\mathrm{d}W}{\mathrm{d}t} \propto P - P_0.$$

At long times, factors different from turgor likely also play a role for variations of cell width.

Supplementary References

1. P. A. J. De Boer, R. E. Crossley, L. I. Rothfield, Central role for the Escherichia coli minC gene product in two different cell division-inhibition systems. *Proceedings of the National Academy of Sciences of the United States of America* **87**, 1129–1133 (1990).

2. C. T. Chung, S. L. Niemela, R. H. Miller, One-step preparation of competent Escherichia coli: transformation and storage of bacterial cells in the same solution. *Proceedings of the National Academy of Sciences of the United States of America* **86**, 2172–2175 (1989).

3. J. A. Valkenburg, C. L. Woldringh, Phase separation between nucleoid and cytoplasm in Escherichia coli as defined by immersive refractometry. *Journal of bacteriology* **160**, 1151–7 (1984).

4. B. Rappaz, *et al.*, Measurement of the integral refractive index and dynamic cell morphometry of living cells with digital holographic microscopy. *Optics Express* **13**, 9361 (2005).

5. H. Makinoshima, A. Nishimura, A. Ishihama, Fractionation of Escherichia coli cell populations at different stages during growth transition to stationary phase. *Molecular Microbiology* **43**, 269–279 (2002).

6. F. Feijó Delgado, *et al.*, Intracellular Water Exchange for Measuring the Dry Mass, Water Mass and Changes in Chemical Composition of Living Cells. *PLoS ONE* **8**, e67590 (2013).

7. D. S. Cayley, H. J. Guttman, M. T. Record, Biophysical characterization of changes in amounts and activity of Escherichia coli cell and compartment water and turgor pressure in response to osmotic stress. *Biophysical journal* **78**, 1748–64 (2000).

8. Z. Wang, *et al.*, Spatial light interference microscopy (SLIM). *Optics Express* **19**, 1016 (2011).

9. A. Edelstein, N. Amodaj, K. Hoover, R. Vale, N. Stuurman, *Computer control of microscopes using manager* (John Wiley & Sons, Ltd, 2010).

10. Z. Wang, G. Popescu, "SPATIAL LIGHT INTERFERENCE MICROSCOPY AND APPLICATIONS," University of Illinois. (2011).

11. M. Mir, B. Bhaduri, R. Wang, R. Zhu, G. Popescu, "Quantitative Phase Imaging" in *Progress in Optics*, (2012), pp. 133–217.

12. G. Popescu, *et al.*, Fourier phase microscopy for investigation of biological structures and dynamics. *Optics Letters* **29**, 2503 (2004).

13. T. H. Nguyen, *et al.*, Halo-free Phase Contrast Microscopy. *Scientific Reports* **7**, 44034 (2017).

14. T. S. Ursell, *et al.*, Rapid, precise quantification of bacterial cellular dimensions across a genomic-scale knockout library. *BMC Biology* **15**, 17 (2017).

15. T. Pilizota, J. W. Shaevitz, Fast, multiphase volume adaptation to hyperosmotic shock by Escherichia coli. *PLoS ONE* **7**, e35205–e35205 (2012).

16. S. B. Mehta, R. Oldenbourg, Image simulation for biological microscopy: microlith. *Biomedical Optics Express* **5**, 1822 (2014).

17. S. B. Mehta, C. J. R. Sheppard, Using the phase-space imager to analyze partially coherent imaging systems: bright-field, phase contrast, differential interference contrast, differential phase contrast, and spiral phase contrast. *Journal of Modern Optics* **57**, 718–739 (2010).

18. J. A. Valkenburg, C. L. Woldringh, Phase separation between nucleoid and cytoplasm in Escherichia coli as defined by immersive refractometry. *Journal of Bacteriology* **160**, 1151–1157 (1984).

19. R. Barer, Interference Microscopy and Mass Determination. *Nature* **169**, 366–367 (1952).

20. G. E. Perlmann, L. G. Longsworth, The Specific Refractive Increment of Some Purified Proteins. *Journal of the American Chemical Society* **70**, 2719–2724 (1948).

21. R. Barer, S. JOSEPH, Refractometry of Living Cells Part I. Basic Principles. *Journal of Cell Science* **s3-95** (1954).

22. G. Popescu, *et al.*, Optical imaging of cell mass and growth dynamics. *AJP: Cell Physiology* **295**, C538–C544 (2008).

23. F. Neidhardt, *et al.*, *Physiology of the bacterial cell: a molecular approach*, J. Simpson, Ed., 1st Ed. (Sinauer Associates Inc, Sunderland, MA, 1990).

24. R. Barer, "PHASE CONTRAST AND INTERFERENCE MICROSCOPY IN CYTOLOGY" in *Cells and Tissues*, (Elsevier, 1956), pp. 29–90.

25. A. Theisen, *Refractive increment data-book for polymer and biomolecular scientists* (Nottingham University Press, 2000).

26. R. E. Marquis, Immersion refractometry of isolated bacterial cell walls. *Journal of bacteriology* **116**, 1273–9 (1973).

27. R. Barer, S. JOSEPH, Refractometry of Living Cells Part I. Basic Principles. *Journal of Cell Science* **s3-95** (1954).

28. G. Churchward, H. Bremer, R. Young, Macromolecular composition of bacteria. *Journal of Theoretical Biology* **94**, 651–670 (1982).

29. E. Fujiwara, T. D. Cabral, M. Sato, H. Oku, C. M. B. Cordeiro, Agarose-based structured optical fibre. *Scientific Reports* **10**, 7035 (2020).

30. M. Mir, *et al.*, Optical measurement of cycle-dependent cell growth. *Proceedings of the National Academy of Sciences* **108**, 13124–13129 (2011).

31. M. Godin, *et al.*, Using buoyant mass to measure the growth of single cells. *Nature Methods* **7**, 387–390 (2010).

32. E. A. Guggenheim, The diffusion coefficient of sodium chloride. *Transactions of the Faraday Society* **50**, 1048 (1954).

33. M. B. Elowitz, M. G. surette, P. E. Wolf, J. B. Stock, S. leibler, Protein mobility in the cytoplasm of Escherichia coli. *Journal of Bacteriology* **181**, 197–203 (1999).

34. E. Soupene, *et al.*, Physiological Studies of Escherichia coli Strain MG1655: Growth Defects and Apparent Cross-Regulation of Gene Expression. *Journal of Bacteriology* **185**, 5611–5626 (2003).

Supplementary Tables

Table S1: Strain list

Strain	Genotype	Construction
E. coli MG1655	WT	Gift from Ghigo lab (Institut Pasteur) (CGSC#6300)
E. coli NCM3722	WT	Gift from Rabinowitz lab (Princeton) (34)
E. coli S290	MG1655/pDB192	MG1655 → pDB192
C. crescentus CB15	WT	Gift from Gitai lab (Princeton University)

Table S2: Number of cells for snapshot experiments

* Different numbers correspond to the different measurements in the corresponding figure (from left to right)

† Combined numbers of cells from two identical replicates.

Experiment	Figure	Strain	*N**
Growth curve	1D	MG1655	11, 22, 95, 80, 115, 42, 170, 301, 142, 197
Osmolallities	1E	MG1655	391, 760
Nutrients	2B-F, S6	MG1655	1243 (MM+mannose), 515 (MM+glycerol), 278 (MM+gluc), 260(MM+gluc+CAA), 97(RDM) †
Nutrients	S6	NCM3722	969 (MM+mannose), 849 (MM+glycerol), 202 (MM+gluc), 614(MM+gluc+CAA), 62(RDM) †
C. crescentus WT	2G-I	CB15	633
A22	3A-C	S290	(see Table S3)
A22	3G	S290	52 (t=0 min), 27 (t=30), 29 (t=60), 43 (t=90)
A22	3I	CB15	228 (t=0 min), 71 (t=60), 77 (t=120), 74 (t=180)
Batch upshift	4A	MG1655	> 460 for every time point
Batch downshift	4C	MG1655	> 88 for every time point

Table S3: Microscopy conditions for time-lapse experiments

Conditions of all time-lapse microscopy experiments including experiment type, corresponding figures, strain, pre-shift ('Medium #1') and post-shift media ('Medium #2'), interval between images (Δt), standard deviation of the Gauss filter (σ), time point of placing cells on the microscope support (t_{exp}) relative to time indicated in figure axis, number of cells (n_{cells}), and microscopy support (agarose pad: 'pad', flow chamber: 'chamber'). If not indicated, *sulA* was induced at t_{exp}.

* Medium prior to osmotic shift: MM+glucose+CAA

** n_{cells} increased with time. At t = -30min, $n_{cells} > 20$

† for these experiments, σ indicates the width of a smoothing average filter

NA Not applicable

†† Drug was already contained in the agar pad. Time $t_{exp} = 0$ min indicates placement of pad onto cells.

& Ramp experiments with first pad with thickness h_1 and Medium #1 covered by second pad with thickness h_2 and Medium #2 at time t=0. c_i and c_f are initial and calculated final concentration after equilibration of NaCl.

Experiment	Figures	Strain	Medium #1	Medium #2	Δt (min)	σ (steps)	t_{exp} (min)	n_{cells}	support
Osmotic shock	1C	S290	MM*	+ NaCl (200mM)	1	0	-60	75	chamber
Filamentation	2D,E; S8	290	MM+glu+CAA	NA	1	25†	0	45	chamber
Division	2F; S8	MG1655	MM+glu+CAA	NA	1.1	0	NA	49**	pad
Upshift #1	4B; S11; S17; 5	S290	MM+mannose	MM+glu+CAA	1.4	1.6	-101	40	chamber
Upshift #2	S11; S16; S17; 5	S290	MM+glu	RDM	1.4	0.6	-106	40	chamber
Downshift	4D; S11; 5	S290	MM+glu+CAA	MM+ mannose	1.4	1.6	-40	25	chamber
correlations	S14; S18	S290	RDM	NA	1.8	7†	-27	108	pad
Control #1	S10	S290	MM+mannose	NA	1.4	9†	-101	35	chamber
Control #2	S10	S290	MM+glu	NA	1.2	9†	-106	130	chamber
Control #3	S10	S290	MM+glu+CAA	NA	1.4	9†	-40	26	chamber
DNP	S19	S290	RDM	+DNP (2 mM)	1.2	0	0††	20	pad
Control	3A-C	S290	MM+glu+CAA	MM+glu+CAA	NA	NA	-10	184	chamber
Filamentation	3A-C	S290	MM+glu+CAA	+1mM IPTG for 75min	NA	NA	-10	44	chamber
A22	3A-C	S290	MM+glu+CAA	+A22 for 70min	NA	NA	-10	87	chamber
A22 +Filamentation	3A-C	S290	MM+glu+CAA	+1mM IPTG +A22 (20ug/ml)	NA	NA	-10	72	chamber
A22 +Filamentation	3D-F; S13	S290	RDM	+1mM IPTG +A22(20ug/ml)	1.2	0.5	0††	37	pad
Control	S10A	S290	RDM	NA	1.8	0.5	0††	103	pad
Hypo-osmotic shock	S17	S290	RDM+NaCl (740mOsm)	RDM (220mOsm)	0.1	0	-10	55	chamber
Hypo-osmotic ramp (c_i=700-> c_f =325mOsm)	6; S21C,D,G	S290	RDM+NaCl (702mOsm)	RDM (200mOsm)	1	0	-24	27	Pad& (h_1=1mm; h_2=3mm)
Hyper-osmotic ramp (c_i =200-> c_f 575mOsm)	6; S21J	S290	RDM (200mOsm)	RDM+NaCl (702mOsm)	1	0	-34	14	Pad& (h_1=1mm; h_2=3mm)
Hypo-osmotic (c_i =1080-> c_f =330mOsm)	S21C,D,F	S290	LB+NaCl (1080mOsm)	LB (80mOsm)	1	0	-47	11	Pad& (h_1=1mm; h_2=3mm)

Hypo-osmotic ramp (c_i=700-> c_f =450mOsm)	6; S21H	S290	RDM+NaCl (702mOsm)	RDM (200mOsm)	1	0	-16	16	Pad[&] (h_1=3mm; h_2=3mm)
Osmotic ramp control (c_i =700-> c_f =700mOsm)	S21C,D,I	S290	RDM+NaCl (697mOsm)	RDM+NaCl (697mOsm)	1	0	-24	26	Pad[&] (h_1=1mm; h_2=3mm)
Immersive refractometry	S4; S9	S290	MM+glu+CAA (280mOsm)	MM+glu+CAA + Dextran (20% w/v)	0.3	0	-15	29	pad

Table S4: Conversion factors for relative changes

Conversion factors used to normalize ρ, *S/M*, *S/V*, and *W* in plots depicting relative changes, including experiment type, corresponding figures, strain, medium, normalization factors, and microscopy support (agarose pad: 'pad', flow chamber: 'chamber').

* Batch experiments reflect single-cell snapshots on agar pads.

& See Table S3 for description of experiment.

Experiment	**Figures**	**Strain**	**Medium #1**	**ρ** (g/ml)	***S/M*** (um^2/pg)	***S/V*** (1/um)	***W*** (um)	**support**
Filamentation	2D,E; S8	S290	MM+glu+CAA	0.333	16.1	5.34	0.828	chamber
Division	2F; S8	MG1655	MM+glu+CAA	0.339	16.1	5.46	0.832	pad
C. crescentus	2I	CB15	PYE	0.370	21.2	7.86	0.556	pad
A22 +Filamentation	3F; S12	S290	RDM	0.289	15.6	4.50	0.963	pad
A22+Filamentation snapshots	3G	S290	RDM	0.274	16.1	4.41	0.977	pad
C. crescentus A22	3I	CB15	PYE+A22(2ugl /ml)	0.403	19.7	7.93	0.576	pad
Upshift (batch)	4A	MG1655	MM+mannose	0.320	19.0	6.08	0.742	pad*
Upshift #1	4B; S11; S17; 5	S290	MM+mannose	0.329	17.9	5.90	0.743	chamber
Upshift #2	S11; S16; S17; 5	S290	MM+glu	0.332	17.0	5.63	0.770	chamber
Downshift (batch)	4C,E	MG1655	MM+glu+CAA	0.311	17.3	5.37	0.840	pad*
Downshift	4D; S11; 5	S290	MM+glu+CAA	0.323	16.2	5.23	0.839	chamber
Control upshift #1	S10F	S290	MM+mannose	0.309	18.7	5.76	0.758	chamber
Control nutrient upshift #2	S10I	S290	MM+glu	0.337	16.7	5.62	0.775	chamber
Control nutrient downshift #3	S10L	S290	MM+glu+CAA	0.344	15.9	5.43	0.809	chamber
DNP	S19	S290	RDM	0.316	14.4	4.54	0.962	pad
Control DNP	S10C	S290	RDM	0.274	16.4	4.49	0.966	pad
Hypo-osmotic shock	S17	S290	RDM+NaCl (740mOsm)	0.334	14.9	4.97	0.878	chamber
Hypo-osmotic ramp (c_i=700-> c_f =325mOsm)	6; S21C,D,G	S290	RDM+NaCl (702mOsm)	0.303	15.1	4.56	0.940	Pad[&] (h_1=1mm; h_2=3mm)
Hyper-osmotic ramp (c_i =200-> c_f 575mOsm)	6; S21J	S290	RDM (200mOsm)	0.268	16.6	4.43	0.943	Pad[&] (h_1=1mm; h_2=3mm)
Hypo-osmotic ramp (c_i=1080-> c_f =330mOsm)	S21C,D,F	S290	LB+NaCl (1080mOsm)	0.339	12.6	4.27	0.987	Pad[&] (h_1=1mm; h_2=3mm)

Hypo-osmotic ramp (c_i=700-> c_f =450mOsm)	6; S21H	S290	RDM+NaCl (702mOsm)	0.297	15.4	4.56	0.962	Pad[&] (h_1=3mm; h_2=3mm)
Ramp control (c_i=700 -> c_f=700 mOsm)	S21C,D,I	S290	RDM+NaCl (697mOsm)	0.307	15.0	4.61	0.930	Pad[&] (h_1=1mm; h_2=3mm)

Table S5: Refraction increments of different intracellular components for the conversion of integrated phase to dry-mass density

Refraction increments of different solutes and cell-envelope components for wavelengths/wavelength ranges as indicated. Fractions of total dry weight are taken from Neidhardt (23) for *Escherichia coli* B/r strain grown in MM+glucose.

* The refraction increment of carbohydrates is used.
** The refraction increment of KCl is used.
† measurement wavelength of refraction increment

Solute (including references)	**Refraction increment (ml/g):**	**Wavelength† (nm)**	**% of total dry weight**
DNA (24)	0.17 – 0.2	546/589	3.1
RNA (24)	0.168-0.194	546/589	20.4
Proteins (24)	0.185	546/589	55.0
Lipopolysaccharide (25)	0.151	546	3.4
Phospholipid (25)	0.16	not given	9.1
Glycogen (24)	0.15	546	2.5
Cell wall (26)	0.18	589	2.5
Metabolites* (27)	0.14	546	2.9
Ions** (27)	0.12	546/589	1.0

Supplementary Figures

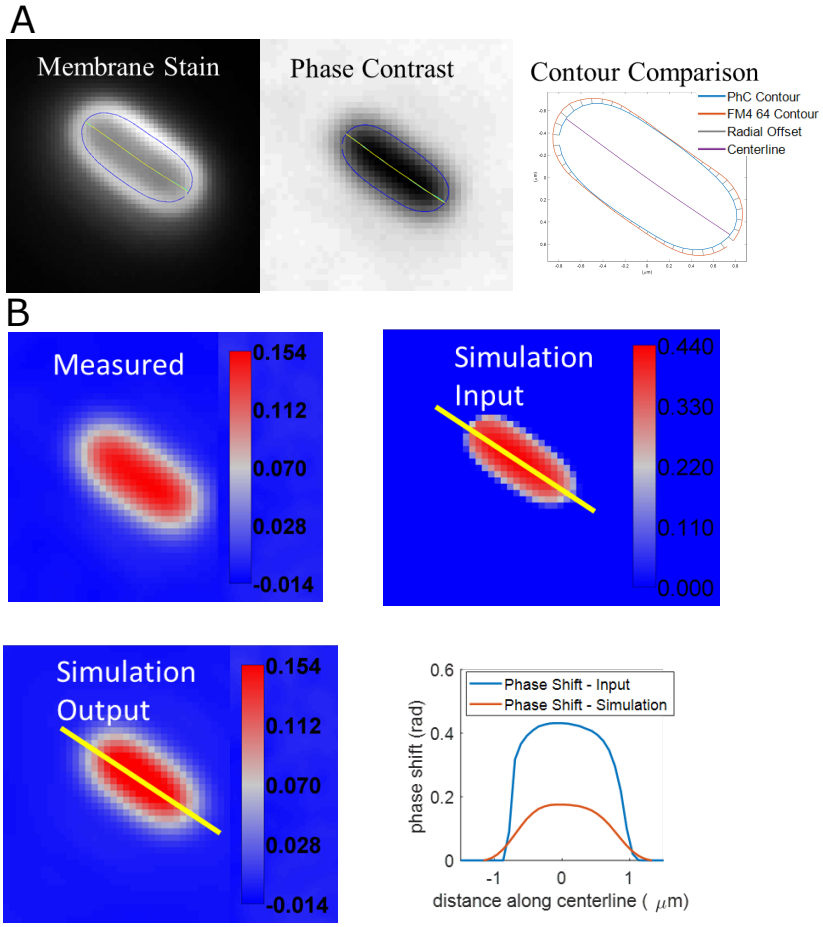

Figure S1. Contour calibration and phase-shift correction. A: Cell contour found from FM4-64 membrane stain (left) and cell contour from phase contrast image (middle) is overlaid (right). Radial offset between contours (grey lines) is measured as a function of distance from the pole. Average radial offsets from n>1000 cells are used to correct contours in all experiments. B: The measured phase image (top left) suffers from optical artifacts. Cell shape found in A is used to create a phase object (simulation input, top right) to simulate the quantitative phase image (simulation output, bottom left). Color scale indicates phase shift. The ratio of integrated phase of the input over the simulated output (bottom right) is used as correction factor for the integrated phase shift from the measured phase image.

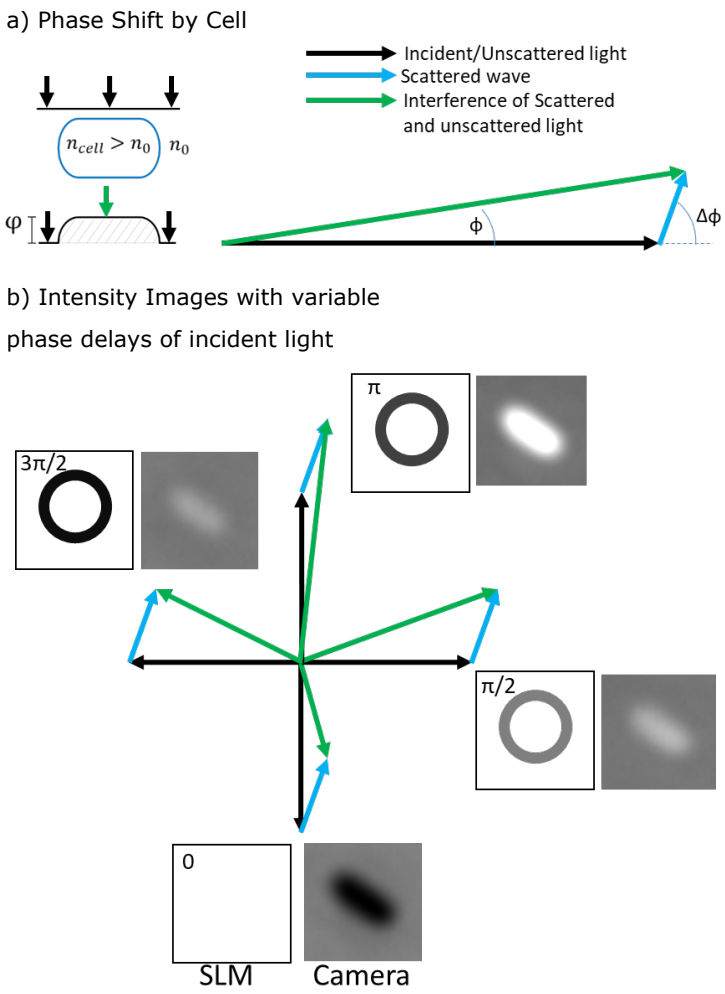

Figure S2. Optical phase shift and intensity-image formation in SLIM. A: Left: A cell with refractive index higher than the surrounding $n_{cell}>n_0$ gives rise to a positive optical phase shift φ. Right: Illustration of resulting wave-vectors. **B:** Analogous to phase-contrast microscopy, the display of the ring on the SLM matching the ring in the objective (c.f. Fig. S3) allows to impart phase delays onto the unscattered light, while the scattered light remains nearly unaffected. Four intensity images with phase delays of λ/4 increments carry sufficient information to reconstruct the optical phase shift of the light travelling through the cell.

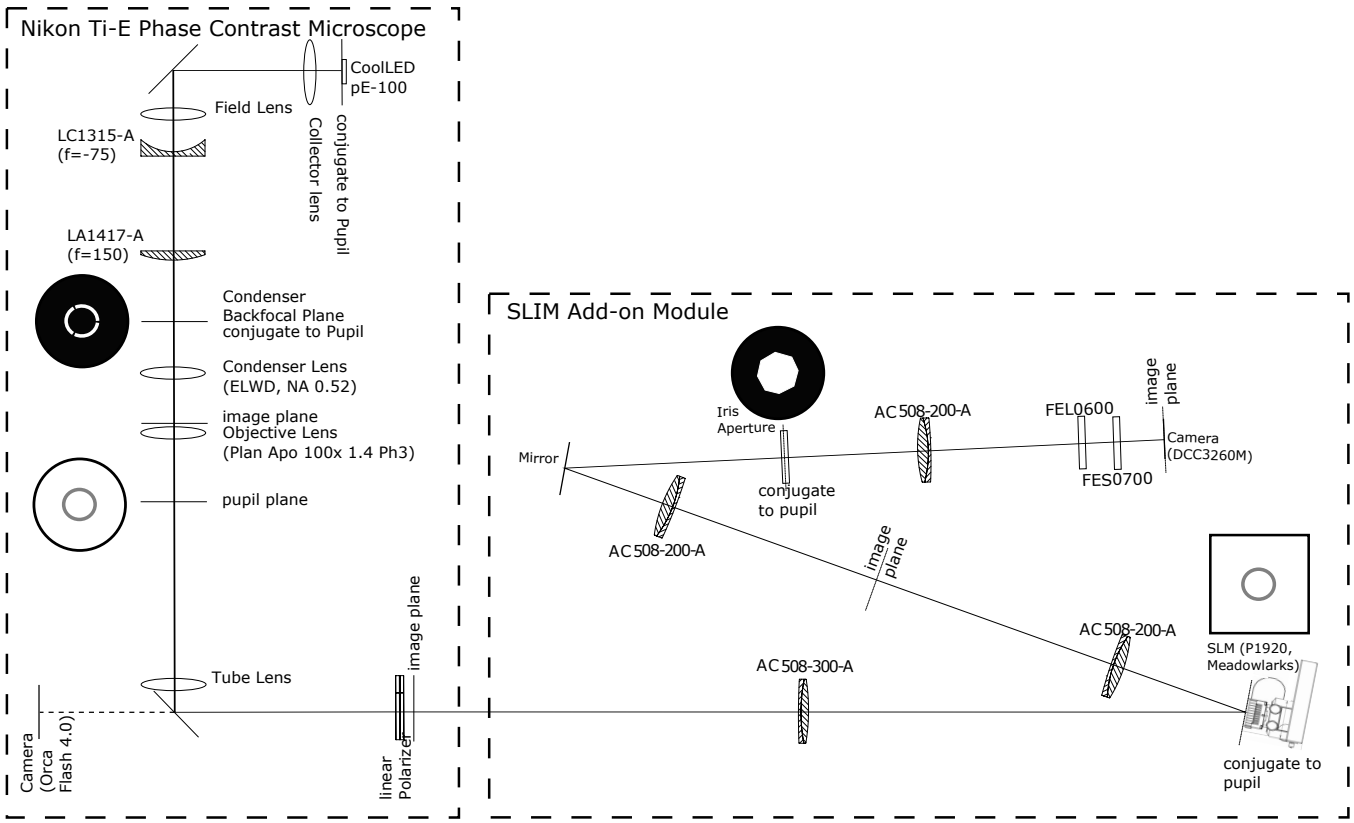

Figure S3. Microscopy setup. Thick dashed boxes indicate the Nikon microscope and the SLIM add-on module. Solid black line indicates optical axis. Next to the conjugate pupil planes a cartoon illustrates the size of: Illumination annulus in the condenser, Phase ring inside the objective, Ring projection on the SLM, and Iris aperture limiting the objective's numerical aperture.

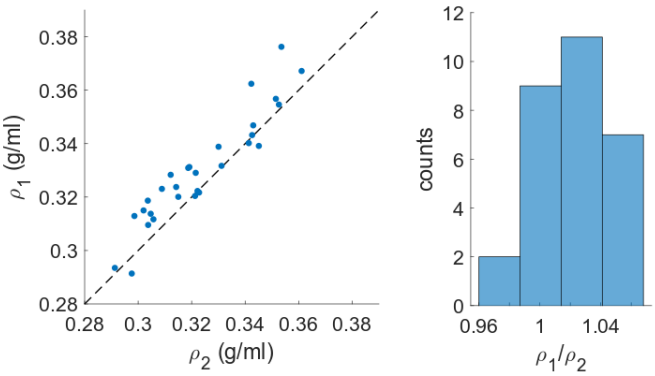

Figure S4. Alternative measurement of mass density through immersive refractometry. We determined dry-mass densities of filamenting cells (S290) growing in MM+Glucose+CAA in a flow chamber in two different ways: In Method 1 we calculate volume based on cell contour and mass based on a single phase image plus simulation-based correction, as described in the main text and in Supplementary note 1 Sections 6-7. In Method 2, referred to as immersive refractometry in the main text, we took two phase images of the same cells before and after changing the refractive index of the medium. We then measured the average refractive index of the cell directly (Supplementary Note 1 Section 11). Both methods give similar results (left panel) with a ratio $\langle \rho_1/\rho_2 \rangle = 1.021 \pm 0.023$ (std). The deterministic offset of 2.1% is within the uncertainty of method 2, due to the uncertainty in measuring the difference in refractive index between the two media. Notably, method 2 does not require an independent volume measurement, nor a correction of the phase signal through simulation. Thus, method 2 validates volume measurement and phase correction in method 1.

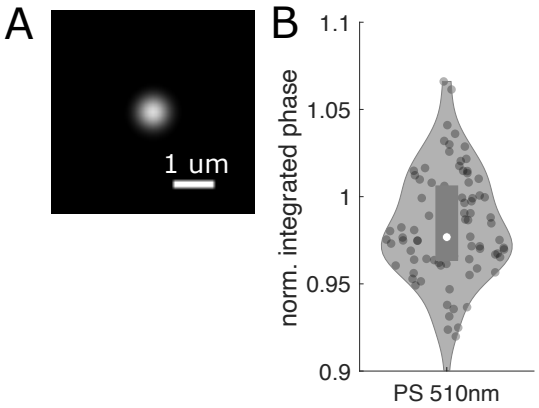

Figure S5. Measurements of latex beads. A. Phase image of a polystyrene latex bead on a 1% agar pad (PolyBeads, PolySciences Inc., 0.51 um diameter, CV=2%). **B.** Distribution of integrated phase (proportional to integrated dry mass and calculated to be the sum of positive phases signal bounded by the negative halo surround the bead), normalized by the expected value according to image simulations of beads of fixed diameter (510 nm) with n_{latex}= 1.5861 and n_{H2O}+n_{agar}= 1.3310+0.0015 (corresponding to n at 635nm and 30C). The deviation in average integrated phase (<2%) and of bead-to-bead variations (CV=3.5%) are within the limits of manufacturing uncertainty (the manufacturer-based CV of 2% in bead diameter corresponds to an expected CV of 6% in volume and thus integrated phase).

(white circle=median; grey rectangle=interquartile range)

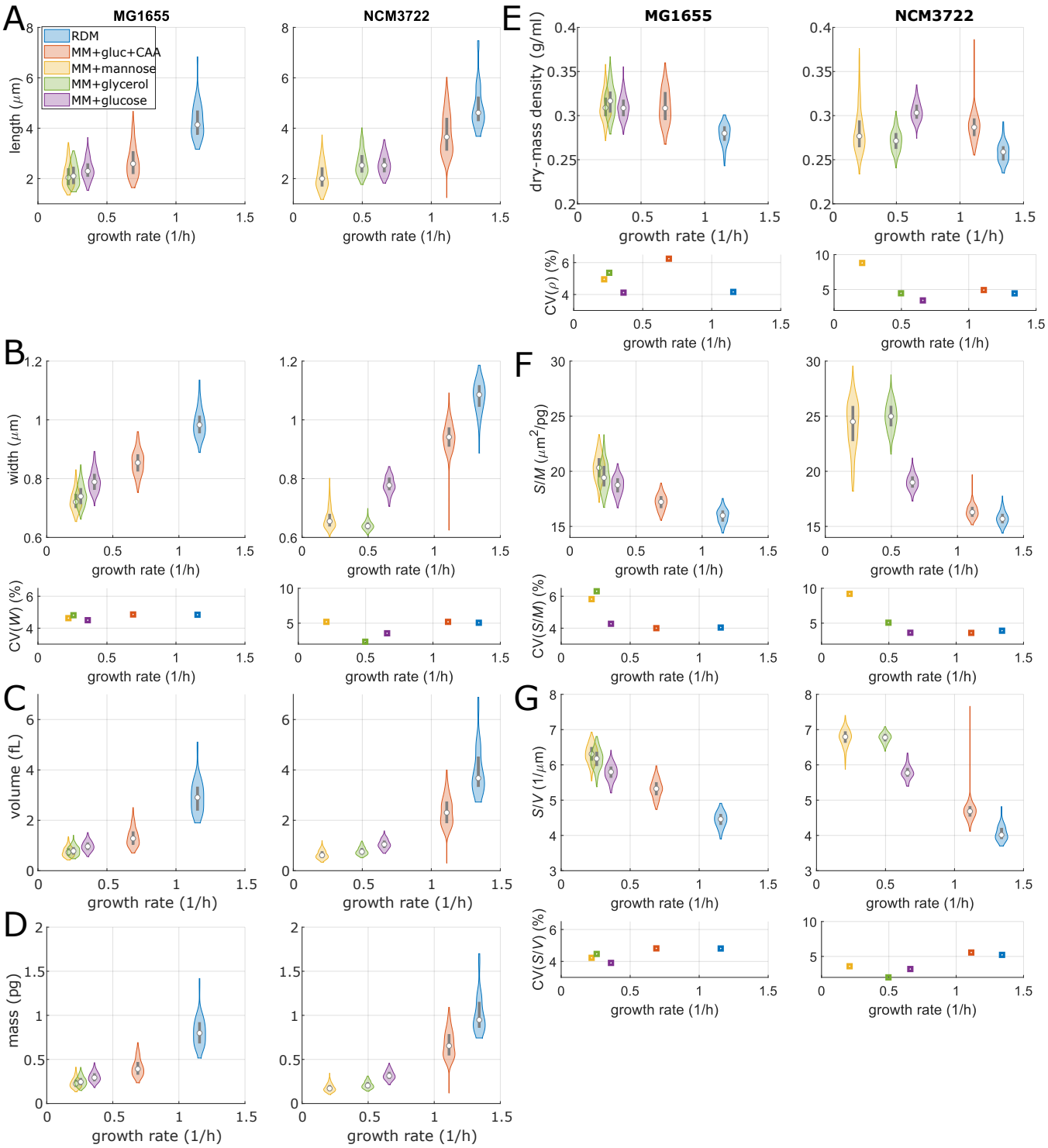

Figure S6. Single-cell properties of MG1655 and NCM3722 during steady-state exponential growth in different nutrient environments. Corresponds to Fig. 2B-C. **A:** Cell length, **B:** Width and its Coefficient of Variation (CV), **C:** Volume, **D:** Mass, **E:** Dry-mass density and CV, **F:** Surface-to-mass ratio and CV, **G:** Surface-to-volume ratio and CV of cells grown to steady-state exponential phase. Number of cells > 62 per condition. (white circles=median; grey rectangles=interquartile range)

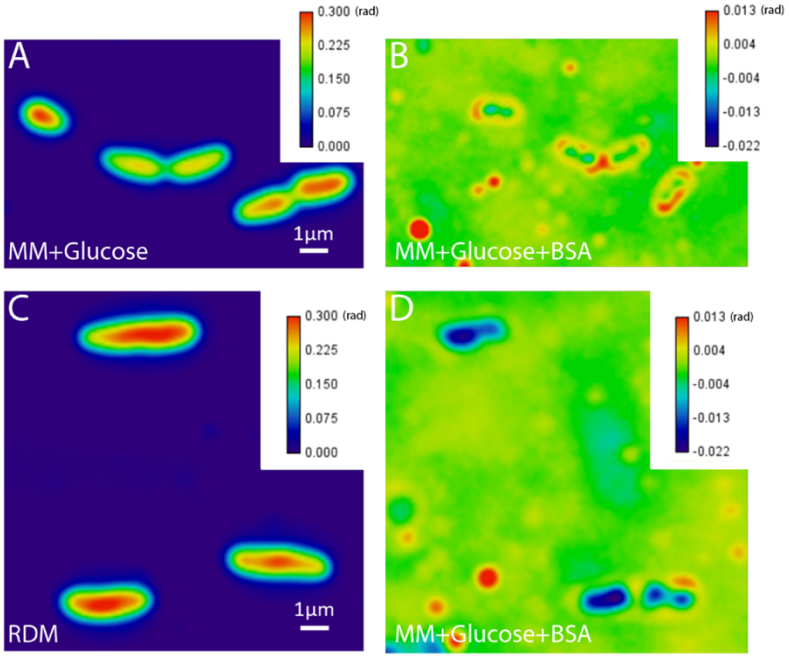

Figure S7. Refractive-index modulation confirms systematic variations in dry-mass density between different media: SLIM images of WT cells (MG1655) grown in either MM+glucose (**A,B**) or RDM (**C,D**) in a flow chamber, before (left) and after (right) exchange to MM+glucose+BSA (n_{medium}=1.384, which corresponds to a dry-mass density of ~0.29g/ml). Note that φ<0, if $n_{cell}<n_{medium}$. In MM+glucose-grown cells, phase shift is zero in the centre and positive (n_{cell}>1.384) for the edges of the cells. In RDM-grown cells, phase shifts is negative (n_{cell}<1.384) for the centre and mainly zero for the edges of the cells. This confirms our measurements based on integrated phase and volume inferred from cell shape (Fig. 2B).

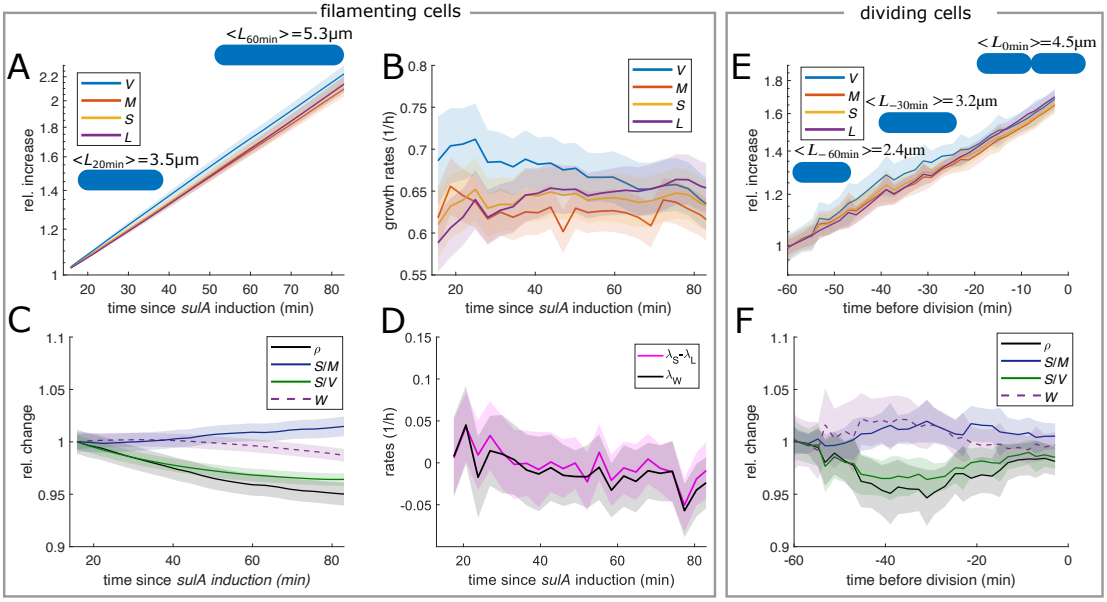

Figure S8. Single-cell time lapse of filamenting cells and dividing cells. A-D: Single-cell time lapse of filamenting cells (S290) in flow chambers (same experiment shown in Fig. 2D,E). **A, B:** Relative increase (A) and single-cell exponential rates $\lambda_X = \mathrm{d}(\log X)/\mathrm{d}t$ (B) of volume, mass, surface, and length. **C:** relative changes of dry-mass density, surface-to-mass- and surface-to-volume ratios, width. **D:** For long spherocylinders with $S \cong \pi LW$, $\lambda_L \cong \lambda_S - \lambda_W$, as is also observed here. Thus, the slight increase of λ_L in over time (B) can be reconciled by the slight decrease of average width in (C), which is possibly a consequence of changing growth conditions from liquid culture to agar pad or induced filamentation. **E-F:** Single-cell time lapse of dividing cells (MG1655) growing on agar pad with MM+glucose+CAA. Single cell traces were aligned in time with respect to their first division, such that $t = 0$ min is time of division. **D:** Relative increase of volume, mass, surface, and length. **F:** Relative changes of dry-mass density, surface-to-mass- and surface-to-volume ratios, width. (solid lines+shadings= average±2*S.E.M.)

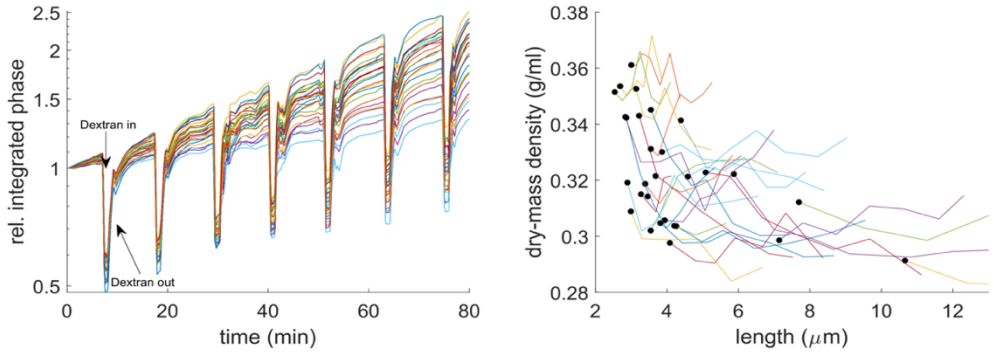

Figure S9. Immersive refractometry confirms length dependency of dry-mass density. Filamenting cells (S290) growing in MM+Glucose+CAA in flow chamber. MM+Glucose+CAA+Dextran with equal osmolality was repeatedly flushed in and out leading to changes in refractive index of the medium and thus changes in integrated phase (**left**). **Right:** Length dependency of dry-mass density. Dry-mass density was inferred from integral refractive index (Supplementary Note 1 Section 11) and was measured repeatedly over the course of one doubling. (black dots=first time point; colored lines=single cell traces)

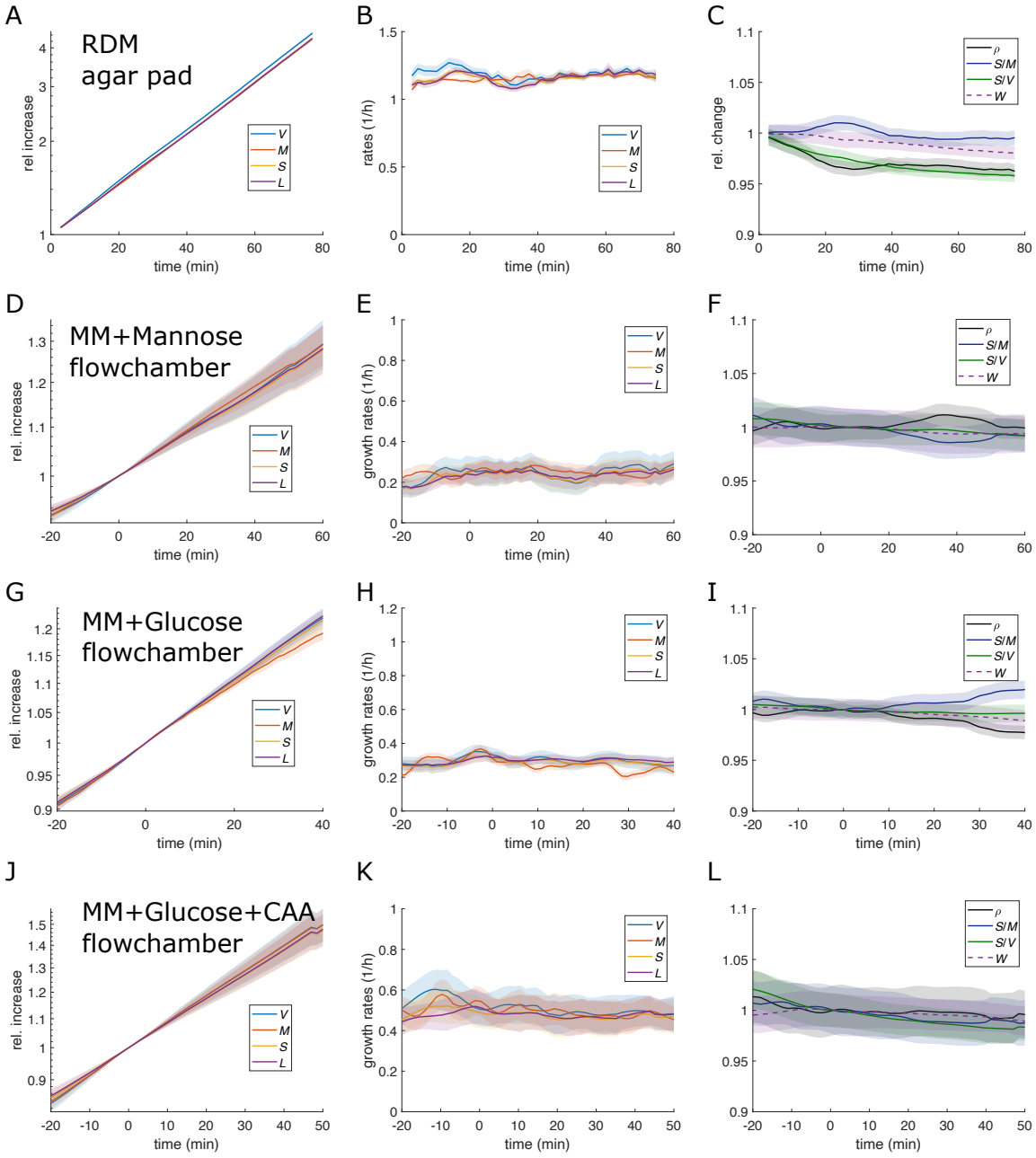

Figure S10. Control experiments for time-lapse drug treatment and nutrient shifts. Single-cell time lapses of filamenting cells (S290) growing on RDM agar (A-C; corresponding to Fig. 2D) and in flow chamber with MM+mannose (D-F; corresponding to Fig. 4B), MM+glucose (G-I; corresponding to Fig. S16), and MM+glucose+CAA (J-L; corresponding to Fig. 4D). From left to right: Relative increase since start of time-lapse (A,D,G,J) and single-cell rates (B,E,H,K) of volume, mass, surface, and length, and relative changes of dry-mass density, surface-to-mass- and surface-to-volume ratios, width (C,F,I,L). For growth on agar pad, time = 0 min corresponds to placement of cells under the pad, while for flow chambers at time = 0 min cells have been growing in the flow chamber for the same time as the corresponding experiments in Fig. 4 and Fig. S16 (solid lines+shadings= average±2*S.E.M.)

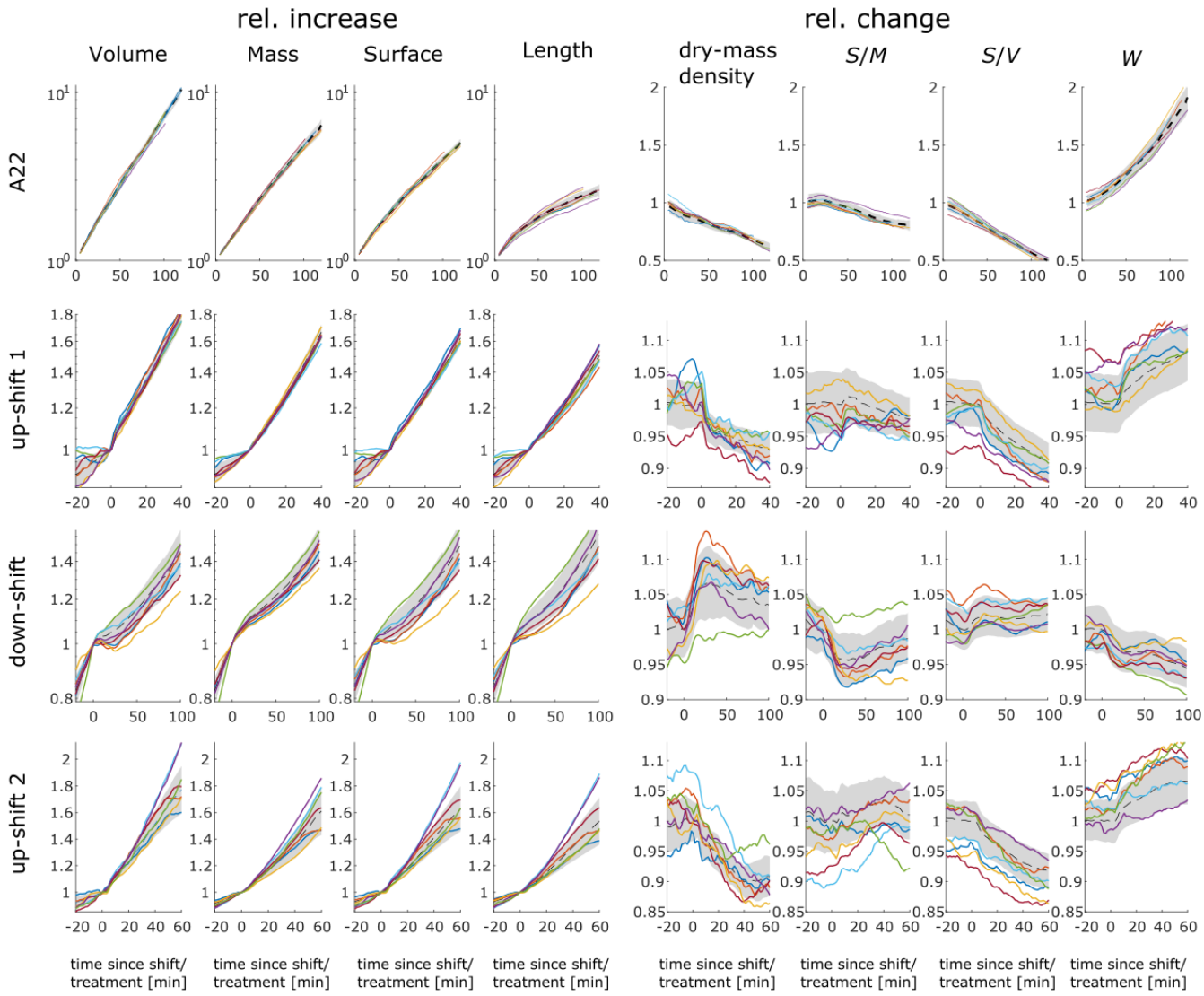

Figure S11. Single-cell traces corresponding to Figs. 3, 4.

Single cell time traces corresponding to average curves from different shifts or perturbations presented in different figures (from top to bottom): A22 treatment (corresponding to Fig 3D-F), nutrient upshift 'up-shift 1' from MM+mannose to MM+glucose+casamino acids (Fig. 4B), nutrient downshift (Fig. 4D), nutrient upshift 'up-shift 2' from MM+glucose to RDM (Fig. S16). For the relative increase (left four columns) of volume, mass, surface, and length, single cell traces were normalized to $t = 0$ min, while for the rel. change (right four columns) of dry-mass density, surface-to-mass ratio, surface-to-volume ratio, and width the average of all traces at $t = 0$min was used for normalization. (dashed lines+shadings= average±STD)

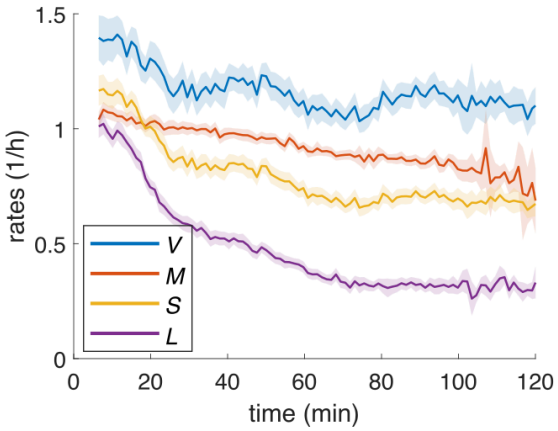

Figure S12. Single-cell rates of volume, mass, surface, and during after A22 treatment. For relative changes of *V*, *M*, *S*, *L*, *ρ*, *S*/*M*, *S*/*V*, *W* see Fig. 3E-F. The reduced surface growth rate after about 20 min of growth under the microscope is likely (at least partially) a compensation of the elevated surface growth rate at the beginning of the time-lapse. (solid lines+shadings= average±2*S.E.M.)

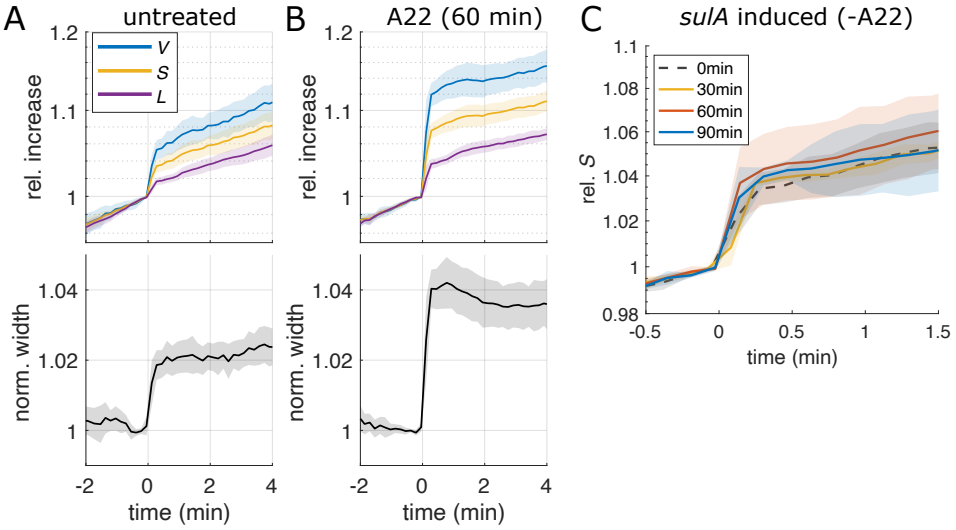

Figure S13. Effect of A22 treatment on turgor pressure. A-B: Relative change of cell dimensions of filamenting cells (S290) during hypo-osmotic shocks realized in flow chambers immediately before (A) and 60 min into (B) combined A22 treatment and *sulA* induction in liquid culture (RDM+glucose). Relative increase of volume, surface, length (top) and width (bottom). Corresponds to Fig. 3H. **C:** relative change of surface area in a control experiment of *sulA* induction only.

(solid lines+shadings= average±2*S.E.M.)

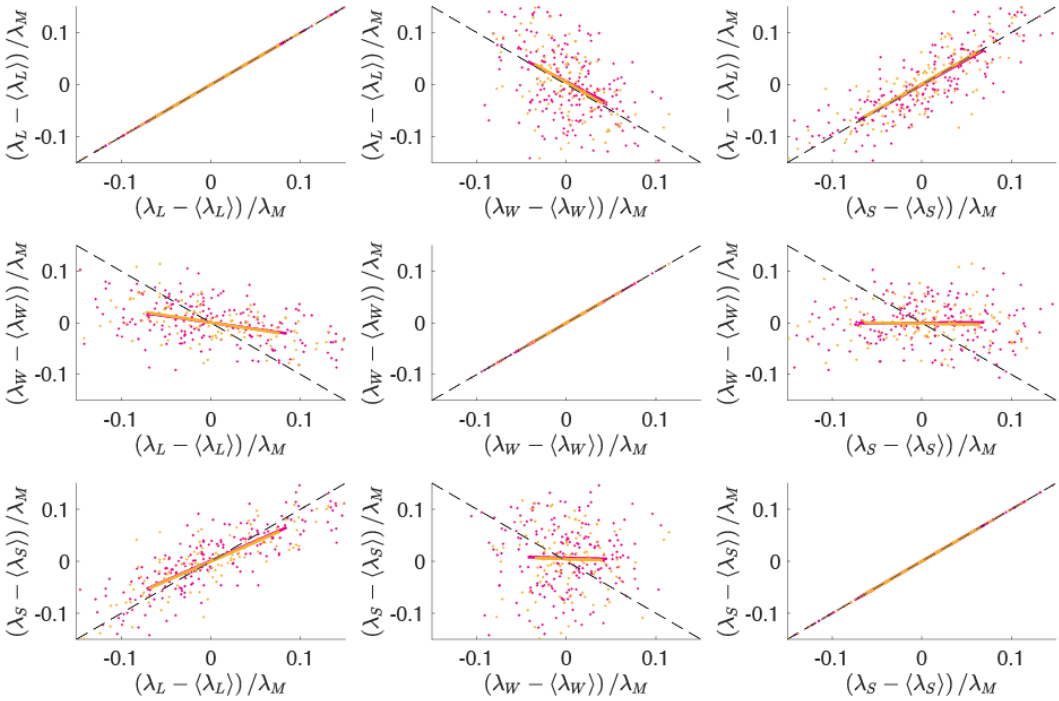

Figure S14. Single-cell correlations support the dependency of elongation rate on surface and widening rates. Matrix of instantaneous correlations between normalized single-cell rates measured from filamenting cells (S290) growing in RDM on agar pad (dots: single-cell measurements of two different replicates (magenta, yellow); colored lines: linear fits; dashed lines: slopes of -1 or +1). Exponential rates are defined as $\lambda_X = \mathrm{d}(\log X)/\mathrm{d}t$ with $X = S, W, L, M$. Since $S = \pi WL$ for spherocylindrical cells, we obtain $\lambda_S = \lambda_L + \lambda_W$. Two colors represent two identical replicates. Lines: linear regression. Fluctuations in λ_L are inversely proportional to fluctuations in λ_W (with a slope of ~-1) and proportional to λ_S (with a slope of ~1) (top row), while λ_W shows hardly any correlations with λ_S or λ_L (middle row). Accordingly, λ_S is also insensitive to variations of λ_W (bottom center), compatible with the hypothesis that λ_L is a function of λ_S and λ_W, according to $\lambda_L(\lambda_W, \lambda_S) = \lambda_S - \lambda_W$, and that λ_S and λ_W are independent of each other.

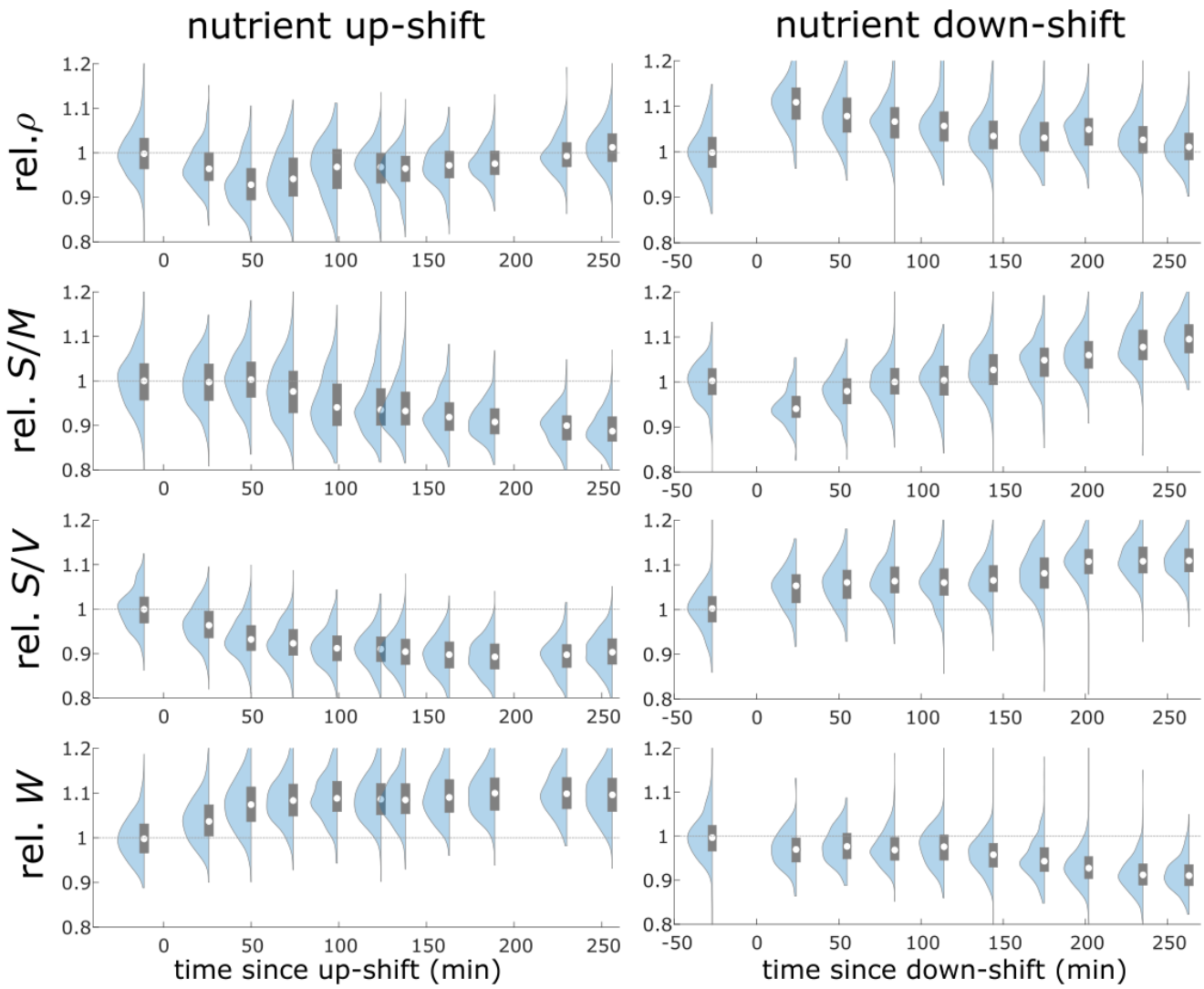

Figure S15. Distributions of mass density, surface-to-mass ratio, surface-to-volume ratio, and width during nutrient upshift and nutrient downshift. Single-cell distributions and median values corresponding to Fig. 4A and Fig. 4C. (Blue shaded distributions = probability density estimates (computed using MATLAB's ksdensity.m function); grey rectangles=interquartile range; white circles=median; *N*>460 cells (up-shift) and *N*>88 cells (down-shift) for each timepoint)

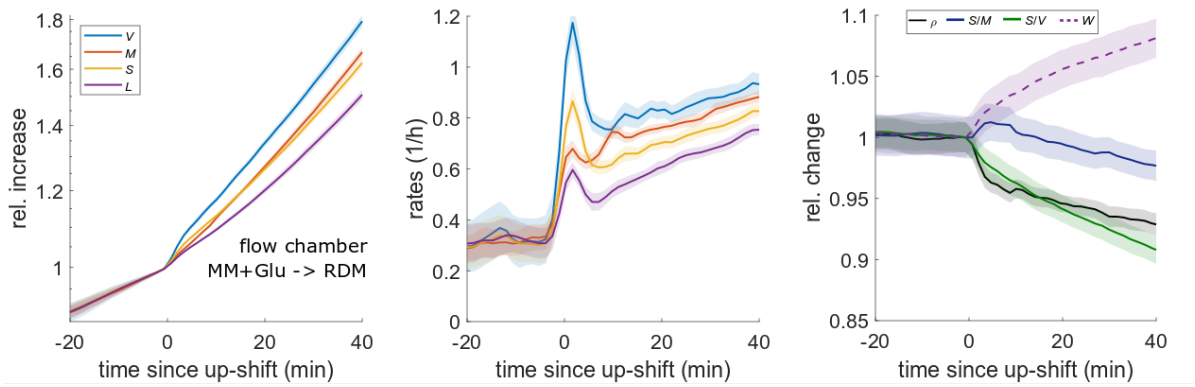

Figure S16. Complementary nutrient upshift in flow channel. Single-cell time lapse of a nutrient upshift from MM+Glu to RDM applied to filamenting cells (S290) in flow chamber. Relative increase (left) and single-cell rates (middle) of volume, mass, surface, and length. Right: Relative changes of dry-mass density, surface-to-mass- and surface-to-volume ratios (for conversion factors see Table S4). (solid lines+shadings= average±2*S.E.M.)

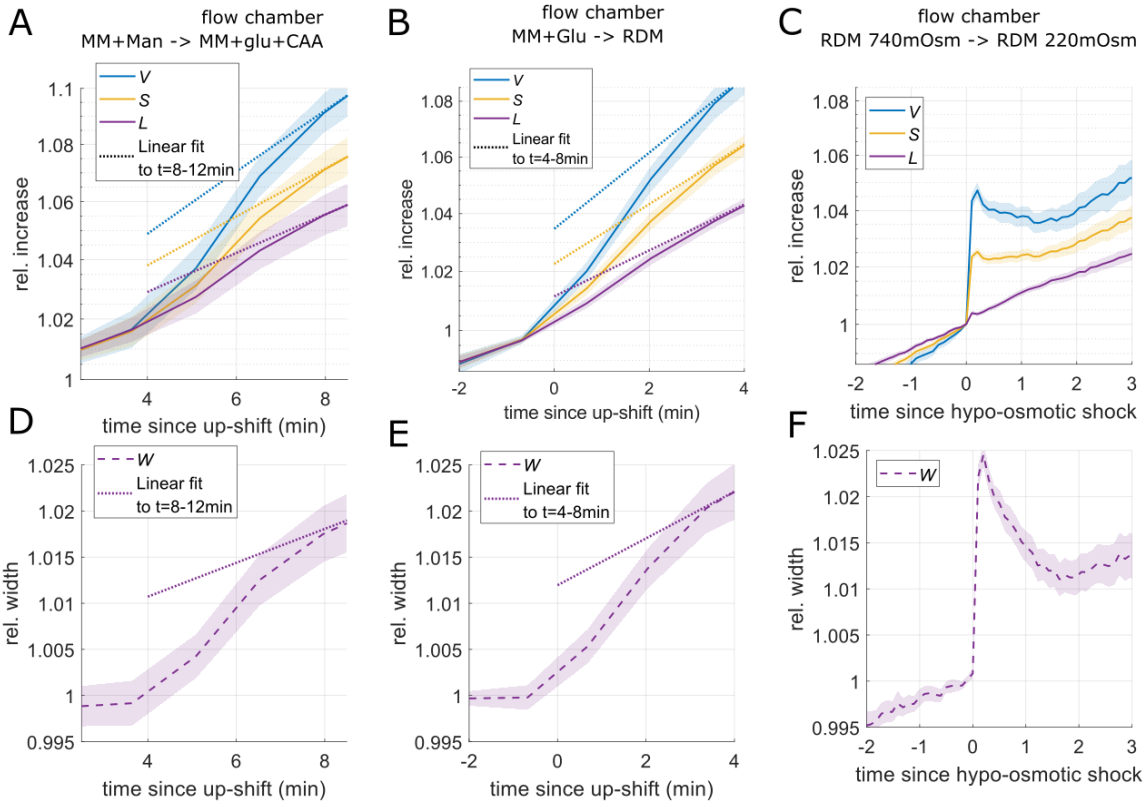

Figure S17. Rapid expansions after nutrient and osmotic shifts. Relative increase of volume, surface and length (**A-C**) and relative change in width (**D-F**) as a function of time after nutrient upshift from MM+mannose to MM+glucose+CAA (**A**,D) and MM+glucose to RDM (**B**,E) (corresponding to Fig. 4B; Fig. S16) and after sudden decrease of osmolality (NaCl based) in RDM from 740mOsm to 220mOsm. Dashed lines are trendlines fitted to the increase after the rapid expansion. After the nutrient upshift, both length and width rapidly increase by >1% within ~ 3 min, which is reminiscent of the expansion during the hypo-osmotic shock. (solid lines+shadings= average±2*S.E.M.)

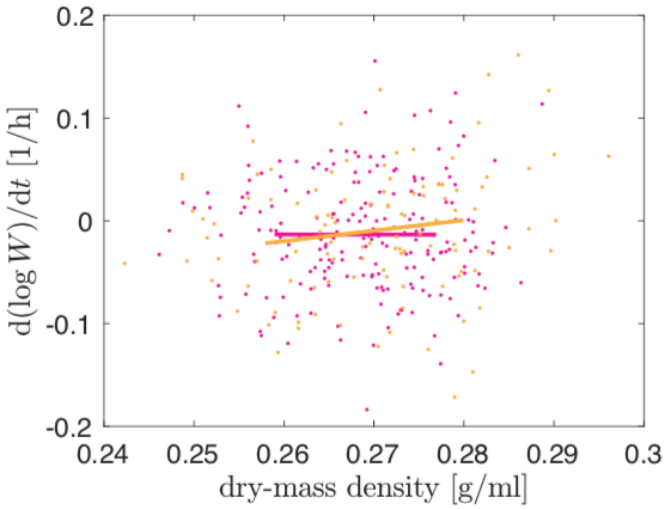

Figure S18. Widening rate is independent of dry-mass density. Instantaneous correlations between exponential widening rate $\lambda_W = \mathrm{d}(\log W)/\mathrm{d}t$ and dry-mass density measured from filamenting cells (S290) growing in RDM on agar pad. (dots: single-cell measurements of two different replicates (magenta, yellow); colored lines: linear fits; dashed lines: slopes of -1 or +1)

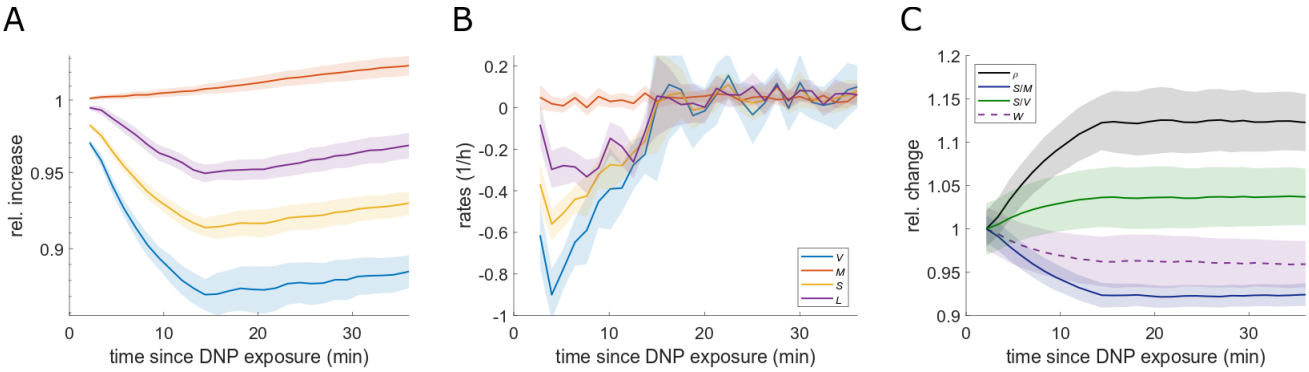

Figure S19. Depletion of ATP and GTP using DNP. Relative change of volume, mass, surface area, length (**A**), relative rates (**B**), and relative changes of dry-mass density, surface-to-mass- and surface-to-volume ratios, width (**C**) as a function of time after exposing filamenting cells (S290) to 2mM 2,4-dinitrophenol (DNP) on a RDM agar pad. (solid lines+shadings= average±2*S.E.M.)

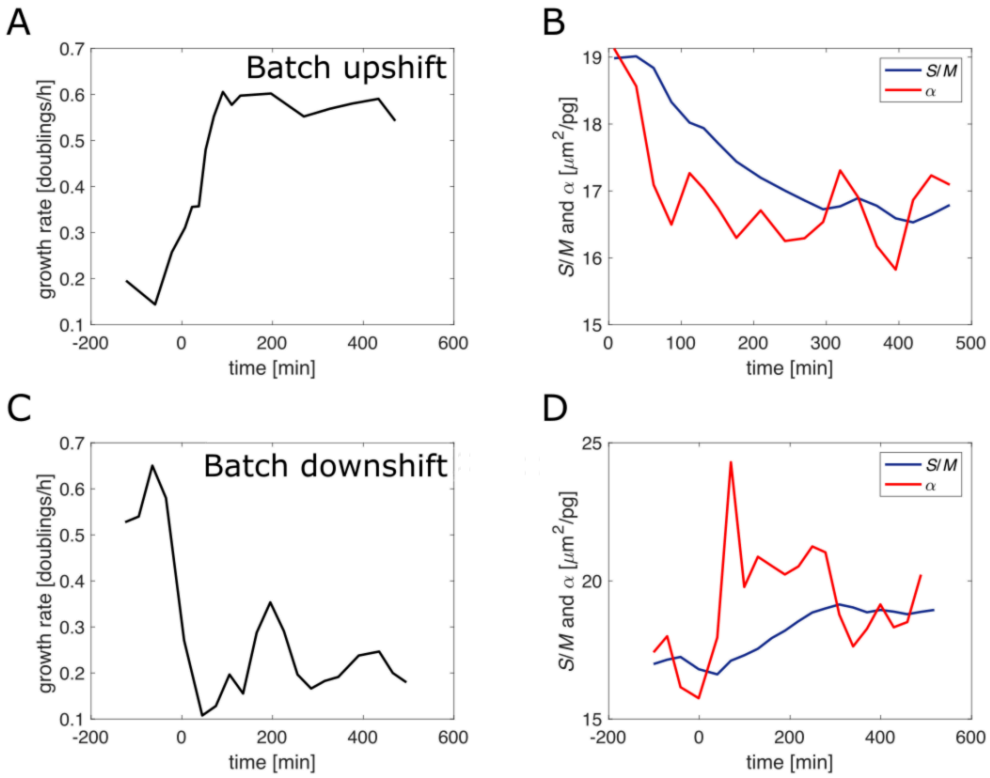

Figure S20. Surface-to-mass coupling constant inferred from batch shifts. A,C: Growth rates from OD600 measurements for batch upshift (A) and downshift (B) already presented in Fig. 4A,C, respectively. **B,D:** Average surface-to-mass ratios and approximate coupling constants $\alpha = \mathrm{d}S/\mathrm{d}M$ inferred from the batch shifts presented in Fig. 4A,C according to $\alpha \approx \lambda_M^{-1}\mathrm{d}\langle S/M\rangle/\mathrm{d}t + \langle S/M\rangle$, where $\lambda_M = \mathrm{d}(\log \mathrm{OD600})/\mathrm{d}t$ is the exponential mass growth rate obtained from OD600 measurements, for upshift (B) and downshift (C). For the calculation of α, we ignored correlations between S/M and λ_M at the single-cell level. The spike in D is likely due to the recovery of turgor pressure after transient reduction of turgor (cf. Fig. 4C).

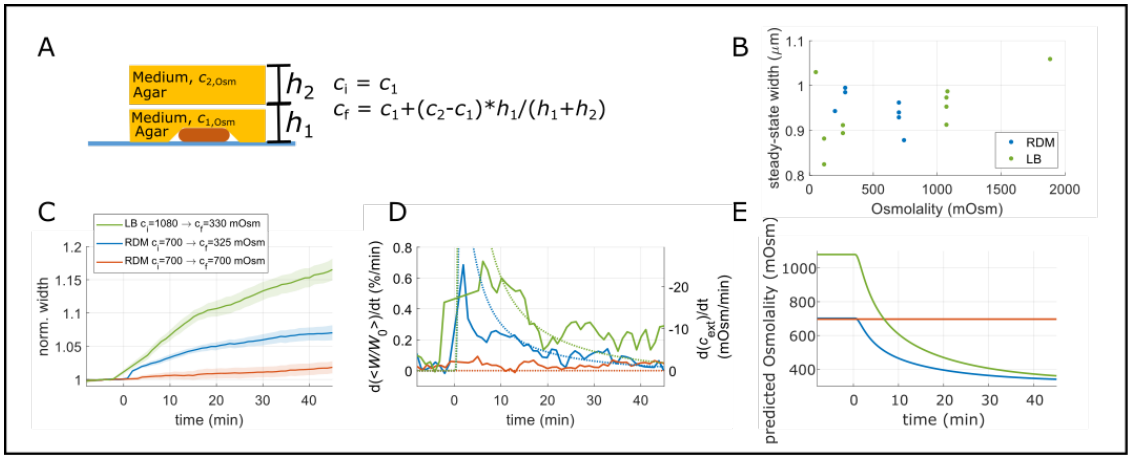
A
Medium, $c_{2,Osm}$
Agar
Medium, $c_{1,Osm}$
Agar
h_2
h_1
$c_i = c_1$
$c_f = c_1+(c_2-c_1)*h_1/(h_1+h_2)$
B
steady-state width (μm)
Osmolality (mOsm)
RDM
LB
C
LB c_i=1080 → c_f=330 mOsm
RDM c_i=700 → c_f=325 mOsm
RDM c_i=700 → c_f=700 mOsm
norm. width
time (min)
D
d(<W/W0>)/dt (%/min)
d(c_{ext})/dt (mOsm/min)
time (min)
E
predicted Osmolality (mOsm)
time (min)

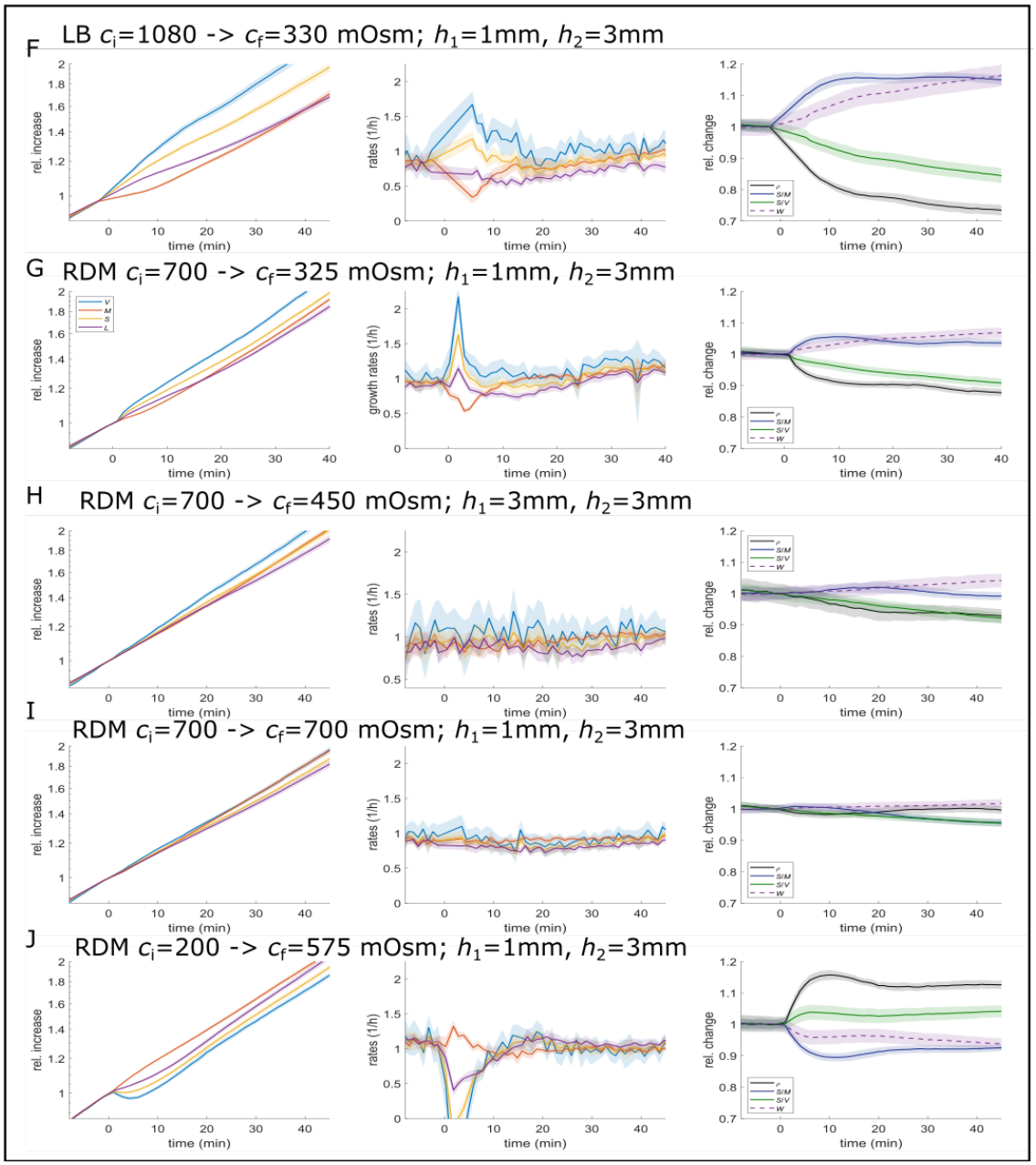
F
LB c_i=1080 -> c_f=330 mOsm; h_1=1mm, h_2=3mm
G
RDM c_i=700 -> c_f=325 mOsm; h_1=1mm, h_2=3mm
H
RDM c_i=700 -> c_f=450 mOsm; h_1=3mm, h_2=3mm
I
RDM c_i=700 -> c_f=700 mOsm; h_1=1mm, h_2=3mm
J
RDM c_i=200 -> c_f=575 mOsm; h_1=1mm, h_2=3mm
rel. increase
growth rates (1/h)
rates (1/h)
rel. change
time (min)
V
M
S
L
S/M
S/V
W

Figure S21. Cell width changes in response to osmotic gradients. A: Illustration of diffusion-based NaCl gradients. Agar pads with different osmolality (NaCl adjusted) are put on top of each other such that diffusion mediates a change in osmolality from initial osmolality c_i to final osmolality c_f. **B:** Average steady-state width of wildtype cells grown in independent LB and RDM cultures with different osmolalities (NaCl adjusted). **C-E:** Normalized cell width (C), rate of widening (solid lines) and rates of osmolality change (dashed lines) (D), the latter are calculated from the predicted osmolality based on 1D diffusion model (E), for filamenting cells (S290) grown in media as indicated in (C). **F-J:** Relative increase of volume, surface, length, and mass (left), exponential rates (middle), and relative change of dry-mass density, surface-to-mass, surface-to-volume, and width (right) for different osmotic gradients in LB (F) and RDM (G-J). (G,H,J) correspond to the width plots for the osmotic gradients in Fig. 6 and (I) corresponds to the control (red).

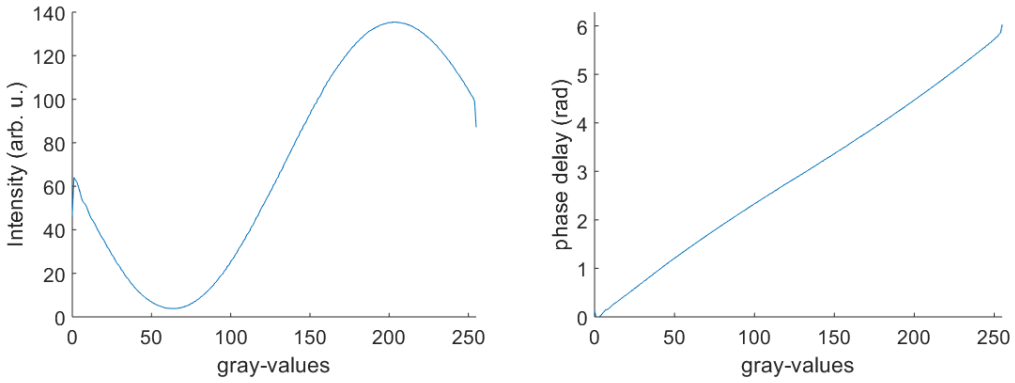

Figure S22. SLM calibration: Intensity response with SLM in amplitude modulation mode (**left**). Conversion of gray-values into phase delay (**right**).

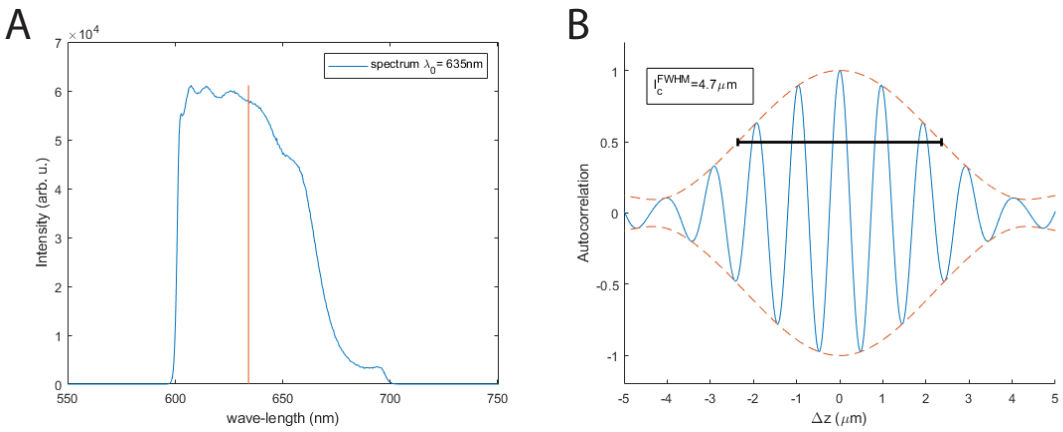

Figure S23. Illumination Spectrum (A) and Autocorrelation (B): White-light illumination source behaves like a monochromatic field with wavelength λ=635nm and a coherence length of less than 5um (black horizontal line in B).

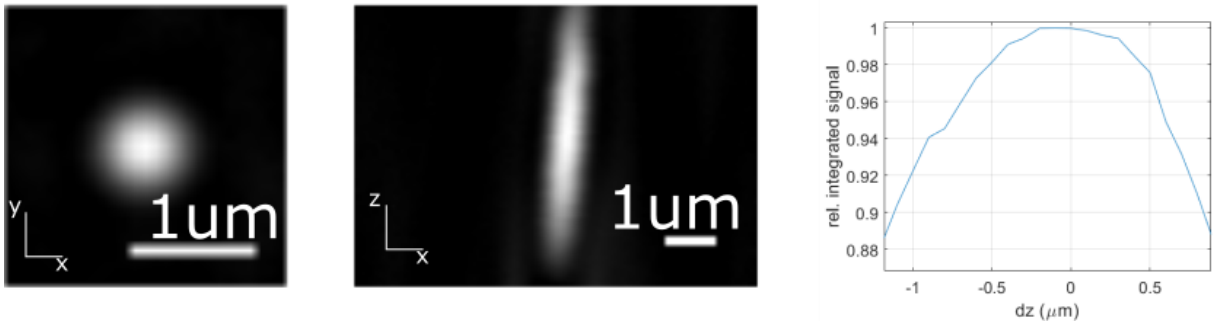

Figure S24. Left: Quantitative phase image of 370nm Polystyrene bead with the objective's effective NA limited to ~0.6. **Middle:** z-projection clearly showing an extended depth of focus. **Right:** Normalized integrated phase of the bead along z.

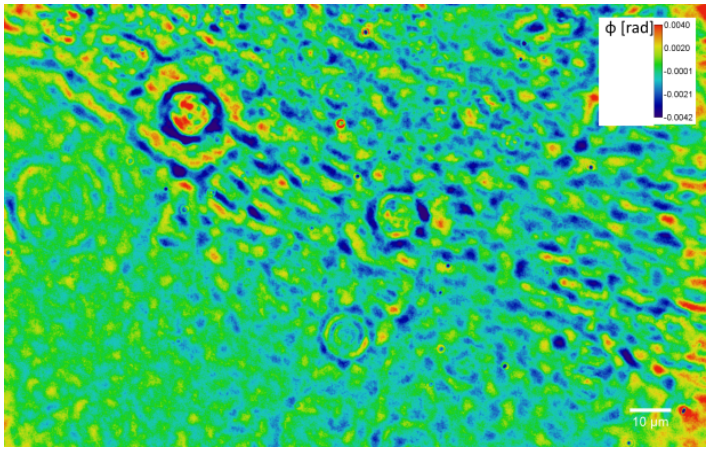

Figure S25. Optical path-length background noise: Pseudo-colored between ±0.004 rad. Scale bar 10 um.

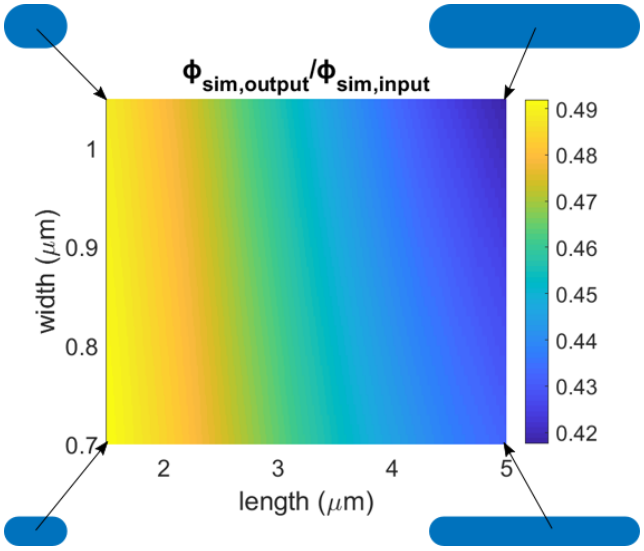

Figure S26. Attenuation of integrated phase ϕ obtained from simulation. Color-code is shown on the right and indicates the ratio $\phi_{sim,output}/\phi_{sim,intput}$. Cartoon cells in the corners illustrate length and width changes.

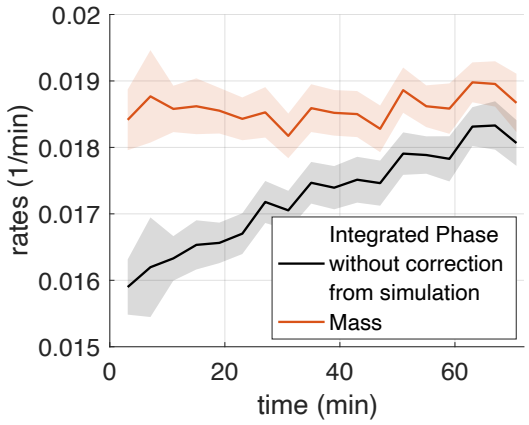

Figure S27. Constant exponential mass growth after correction from simulation. Cells were imaged on an RDM agar pad. (solid lines: avg; shading: SEM; <L(t=0)>=4.6 um; <L(t=75 min)>=18.5 um).

Supplementary Movies

Movie S1: Filamenting cell. Single-cell time lapse of experiment shown in Figs. 2D, E. Time stamps indicate time since induction of *sulA*.

Movie S2: A22 treatment. Single-cell time lapse of experiment shown in Fig. 3D. Time stamps indicate time with respect to covering cells with the A22 containing agar pad. We only considered the first 100 frames (~120 min) for computational analysis (Fig. 3), since cell segmentation becomes faulty afterwards due to the large empty periplasmic space. However, the long-time movie (~240min) demonstrates that cell-surface growth continues seemingly without interruption even though the cytoplasm occupies a decreasing part of the cell volume.

Movie S3: Nutrient upshift from MM+mannose to MM+glucose+CAA. Single-cell time lapse of experiment shown in Fig. 4B. Time stamps indicate time with respect to shift.

Movie S4: Nutrient upshift from MM+glucose to RDM. Single-cell time lapse of experiment shown in Fig. S16. Time stamps indicate time with respect to shift.

Movie S5: Nutrient downshift from MM+glucose+CAA to MM+mannose. Single-cell time lapse of experiment shown in Fig. 4D. Time stamps indicate time with respect to shift.

Movie S6: Depletion of ATP and GTP using DNP. Single-cell time lapse of experiment shown in Fig. S19. Filamenting cell (S290) during ATP and GTP depletion using 2,4-dinitrophenol (DNP) on a RDM agar pad. Time stamps indicate time of placing DNP agar pad onto cells.

Movie S7: Hypo-osmotic ramp. Single-cell time lapse of experiment shown in Fig. 6 (blue line). Time stamps indicate time with respect to placing an agar pad with low NaCl on top of the microscopy agar pad with high NaCl, which leads to a time-dependent reduction of osmolality.